Late Quaternary aggradation and incision in the headwaters of the Yangtze River, eastern Tibet Plateau, China

Yu Yang[1], Wang Xianyan[1], Yi shuangwen[1], Miao Xiaodong[2], Vandenberghe Jef[3], Li Yiquan[4], and Lu Huayu[5]

[1]Nanjing University
[2]School of Resource and Environmental Sciences, Linyi University
[3]VU University
[4]School of Geography and Ocean Science, Nanjing University
[5]School of Geography and Ocean Science, Nanjing University, Nanjing, China

November 16, 2022

Abstract

River aggradation or incision at different spatial-temporal scales are governed by tectonics, climate change and surface processes which all adjust the ratio of sediment load to transport capacity of a channel. But how the river responds to differential tectonic and extreme climate events in a catchment is still poorly understood. Here, we address this issue by reconstructing the distribution, ages and sedimentary process of fluvial terraces in a tectonically active area and monsoonal environment in the headwaters of the Yangtze River in the eastern Tibet Plateau. Field observations, topographic analyses and optically stimulated luminescence (OSL) dating reveal a remarkable fluvial aggradation, followed by terraces formations at elevations of 62-55 m (T7), 42-46 m (T6), 38 m (T5), 22-36 m (T4), 18 m (T3), 11 m (T2), 2-6 m (T1) above the present floodplain. Gravelly fluvial accumulation more than 62 m thick has been dated prior to 24-19 ka. It is regarded as a response to cold climate during the Last Glacial Maximum. Subsequently, the strong monsoon precipitation contributed to cycles of rapid incision and lateral erosion, expressed as cut-in-fill terraces. The correlation of terraces suggests that specific tectonic activity controls the spatial scale and geomorphic characteristics of the terraces, while climate fluctuations determine the valley filling, river incision and terrace formation. Debris and colluvial sediments are frequently interbedded in fluvial sediment sequences, illustrating the episodic short-time blocking of the channel around 20 ka. This indicates the potential impact of extreme events on the geomorphic evolution in the rugged terrain.

Late Quaternary aggradation and incision in the headwaters of the Yangtze River, eastern Tibet Plateau, China

Yang Yu [1], Xianyan Wang [1, *], Shuangwen Yi [1], Xiaodong Miao[2], Jef Vandenberghe [1, 3], Yiquan Li [1], Huayu Lu [1]

[1]School of Geography and Ocean Science, Nanjing University, Nanjing, China

[2]School of Resource and Environmental Sciences, Linyi University, Linyi, China

[3]Department of Earth Sciences, VU University Amsterdam, Amsterdam, The Netherlands

*corresponding author: Xianyan Wang (xianyanwang@nju.edu.cn)

Key Points:

- Fluvial terraces in the headwaters of Yangtze River in east Tibetan Plateau are mapped and dated by OSL method.
- Climate and monsoon fluctuations determine the valley filling and river incision, while tectonic controls the spatial scale of terraces.
- Extreme events show the potential impact on the geomorphic evolution along the high relief margin orogenic plateau in monsoon environment.

Abstract River aggradation or incision at different spatial-temporal scales are governed by tectonics, climate change and surface processes which all adjust the ratio of sediment load to transport capacity of a channel. But how the river responds to differential tectonic and extreme climate events in a catchment is still poorly understood. Here, we address this issue by reconstructing the distribution, ages and sedimentary process of fluvial terraces in a tectonically active area and monsoonal environment in the headwaters of the Yangtze River in the eastern Tibet Plateau. Field observations, topographic analyses and optically stimulated luminescence (OSL) dating reveal a remarkable fluvial aggradation, followed by terraces formations at elevations of 62-55 m (T7), 42-46 m (T6), 38 m (T5), 22-36 m (T4), 18 m (T3), 11 m (T2), 2-6 m (T1) above the present floodplain. Gravelly fluvial accumulation more than 62 m thick has been dated prior to 24-19 ka. It is regarded as a response to cold climate during the Last Glacial Maximum. Subsequently, the strong monsoon precipitation contributed to cycles of rapid incision and lateral erosion, expressed as cut-in-fill terraces. The correlation of terraces suggests that specific tectonic activity controls the spatial scale and geomorphic characteristics of the terraces, while climate fluctuations determine the valley filling, river incision and terrace formation. Debris and colluvial sediments are frequently interbedded in fluvial sediment sequences, illustrating the episodic short-time blocking of the channel around 20 ka. This indicates the potential impact of extreme events on the geomorphic evolution in the rugged terrain.

1. Introduction

Rivers play the most active role in shaping the landscape either by erosion or deposition in a source-to-sink system (e.g. Allen, 2008; Sommé and Jackson, 2013). The river incises or aggrades alternatively through varying discharge, sediment load and channel slope as a response to tectonic activities and/or climatic fluctuations (e.g. Stokes et al., 2018; Vandenberghe et al., 2018; De Paula and Magalhães Jr., 2020). In addition, rivers in rugged mountains with high relief resulting from the interaction of tectonics and climate, are generally vulnerable to extreme events, such as orographically enhanced catastrophic precipitation that may initiate landslides, rock-falls and debris flows, potentially leading to cascading dynamic processes and complex fluvial response (e.g. Molnar et al., 1993, 2013; Srivastava et al., 2008). In such prominent landforms, river damming and dam failure may strongly influence aggradation and incision both in upstream and downstream directions (e.g. Korup et al., 2008; Hewitt et al., 2008). Such accumulation of sediment load due to damming effects may abrade or protect the underlying channel bedrock in orogenic mountains, which has profound effects on the evolution of large rivers and regional landforms (e.g. Korup et al., 2010).

Earlier studies concluded that extreme events, such as earthquakes, extreme rainfall and glacial activities, could lead to damming of rivers or breaking dams in high relief areas (Korup and Tweed, 2007; Handwerger et al., 2019; Fan et al., 2019). Global warming will probably increase the magnitude of climate fluctuations and extreme events, which potentially may cause a series of natural hazards threatening the inhabitants (e.g. Chug et al., 2020). There are plenty of reports about mega-floods or debris flows in the rivers around the Tibet Plateau (e.g. Chen et al., 2007; Wu et al., 2016; Cook et al., 2018; Liu et al., 2015, 2018, 2019). But internal mechanisms and interplays between tectonic, climate and extreme events (such as landslides, debris and rock-falls) in mountains are still obscure and need to be researched at geological timescale.

The geomorphic evolution at the margins of the Tibet Plateau is controlled by rapid and remarkable incision of large rivers, e.g. Jinsha, Mekong and Nujiang Rivers, and intensive landslides, which could be produced by the intensified monsoonal rainfall (e.g. Chen et al., 2008; Kong et al., 2009; Henck et al., 2011; Ferrier et al., 2013; Schanz et al., 2018; Nie et al., 2018; Tao et al., 2020; Bao et al., 2020) (Figure 1). The strong tectonic activities with frequent earthquakes (such as Yushu Ms7.1 in 2010) (e.g. Zhang et al., 2013) and the high relief indicate the upper Yangtze River is vulnerable to extreme processes of landslides and debris flows which may block the valley, leading to the breakage of channel connections in the headwaters of the Yangtze River (e.g. Chen et al., 2008; Bao et al., 2020) (Figure 1A). Thus, fluvial systems in this area with intensive monsoonal precipitation and active tectonics could provide important archives to assess the fluvial response to extreme events.

In this paper, field investigation with description of the sedimentary sequences have been supplemented with OSL dating to establish the terrace sequence and incision rates of the headwaters of the Yangtze River in the eastern Tibet Plateau (ETP) as an example of fluvial response to tectonic movement, climate change and extreme events. More specifically, we report the valley filling and the formation of cut-in-fill terraces during the last deglaciation, as a response to geomorphic processes, climate fluctuations and extreme events in a tectonically active setting.

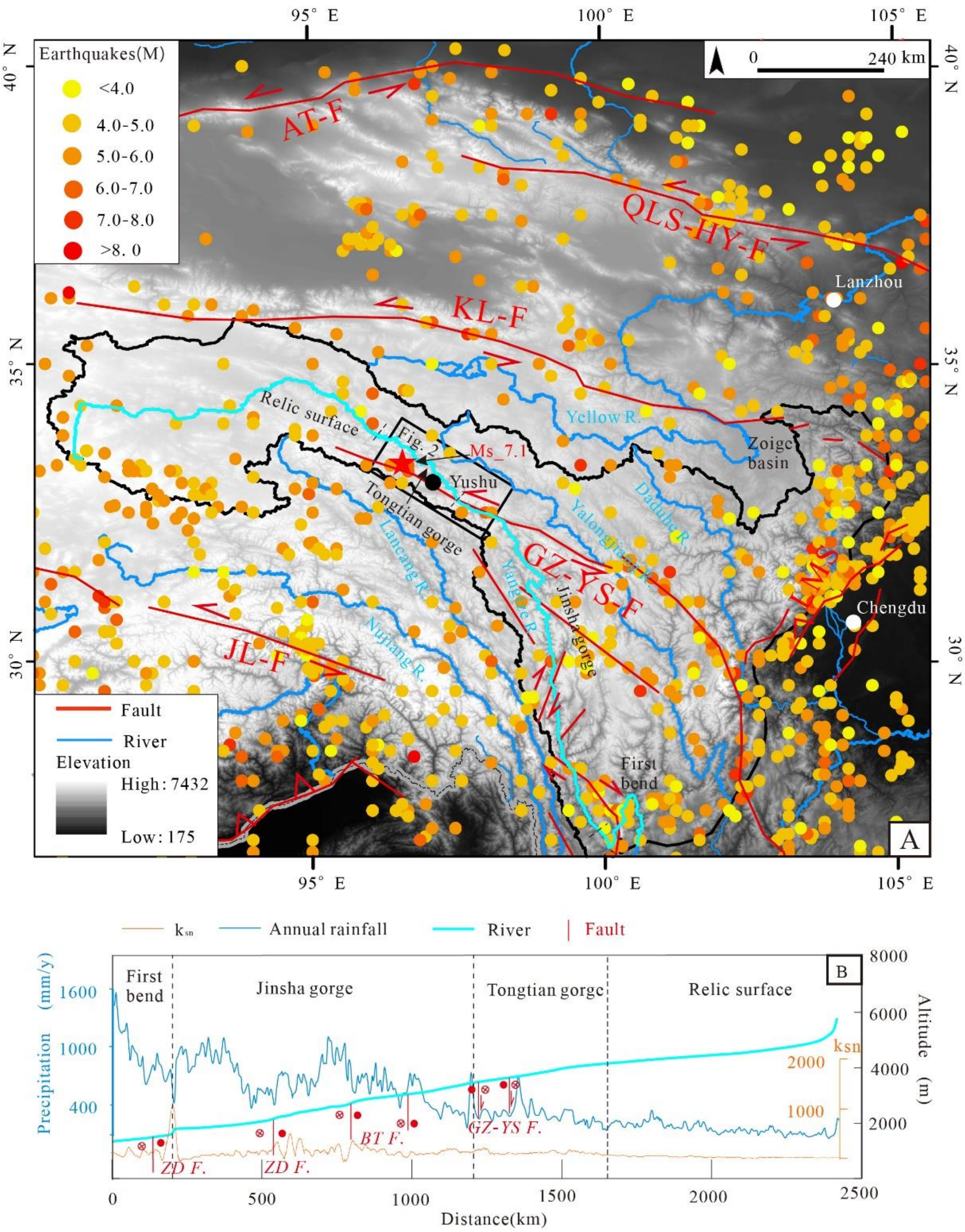

Figure 1. (A) Topographic map of ETP based on the 90-m digital elevation model (DEM) from the Shuttle Radar Topography Mission (SRTM), showing the location of rivers, active faults, and historical earthquakes. The Yangtze River is highlighted by fluorescent-blue, while the other rivers are marked by vivid-blue lines. The black rectangle shows our study area in the headwaters of the Yangtze River. Main strike-slip faults with left-lateral movement are represented from Tapponnier et al. (2001), Deng et al. (2003) and Taylor and Yin (2009). AT-F: Altyn Tagh fault; QLS-HY-F: Qilianshan-Haiyuan fault; KL-F: Kunlun fault; GZ-YS-F: Ganzi-Yushu fault; LMS:

Longmenshan; JL-F: Jiali fault. Historical earthquakes from 780 B.C. to 2018 were collected from China Earthquake Networks Center (http://data.earthquake.cn/index.html). (B) Longitudinal profile of the Yangtze River (fluorescent-blue), TRMM (Tropical Rainfall Measuring Mission)-derived average annual precipitation (vivid-blue, http://www.geog.ucsb.edu/~bodo/TRMM/) and normalized channel steepness (k_{sn}, a geomorphic parameter proportional to incision rate (Kirby et al., 2003)) (brownish-yellow) along the headwaters of the Yangtze River. Black dash lines divide the river valley into broad valleys, Relic surface Tongtian gorge, Jinsha gorge and First bend of Yangtze River. Left-lateral faults and right-lateral active faults intersecting with the Yangtze River are indicated as GZ-YS-F: Ganzi-Yushu fault; BT-F: Batang fault; ZD-F: Zhongdian fault.

2. Geological and Geographic setting

The Ganzi-Yushu fault (GZ-YS-F) is a NW-SE strike-slip fault developed due to the lateral extrusion related to the India-Eurasia collision (Figure 1A). It originates from the Ganzi fault to the southeast and terminates against the Dangjiang fault to the northwest; it extends over about 500 km, tends to the northeast with a dip angle of 70°-85° and coordinates the tectonic activities between the tectonic Qiangtang, Bayankala and Sichuan-Yunnan blocks (Wen et al., 2010; Chen et al., 2010; Wu et al., 2012). The GZ-YS-F provides evidence of active transtensional deformation with stream offsets, fault scarps, pull-apart basins, shutter ridges and earthquakes (Yushu Ms7.1) since the late Quaternary (Figures 1A and 2) (e.g. Wen et al., 1985; Zhou et al., 1997; Wen et al., 2003; Wang et al., 2008). Based on the geometry and historical earthquake data, the GZ-YS-F is divided into Ganzi, Manigange, Dengke, Yushu and Dangjiang segments (e.g. Zhou et al., 1996). This study mainly focuses on the northwestern part of the GZ-YS-F with a series of secondary structures such as folds, normal faults and thrust faults (Figure 2). The general slip movement between Qiangtang and Bayankala blocks led to local fragmentation of the headwaters of the Yangtze River into small blocks of local extent that have subsided and/or uplifted relatively to each other. Fluvial aggradation in the subsiding blocks contrasts with incision and formation of gorges in the uplifted blocks (Figures 2B, C).

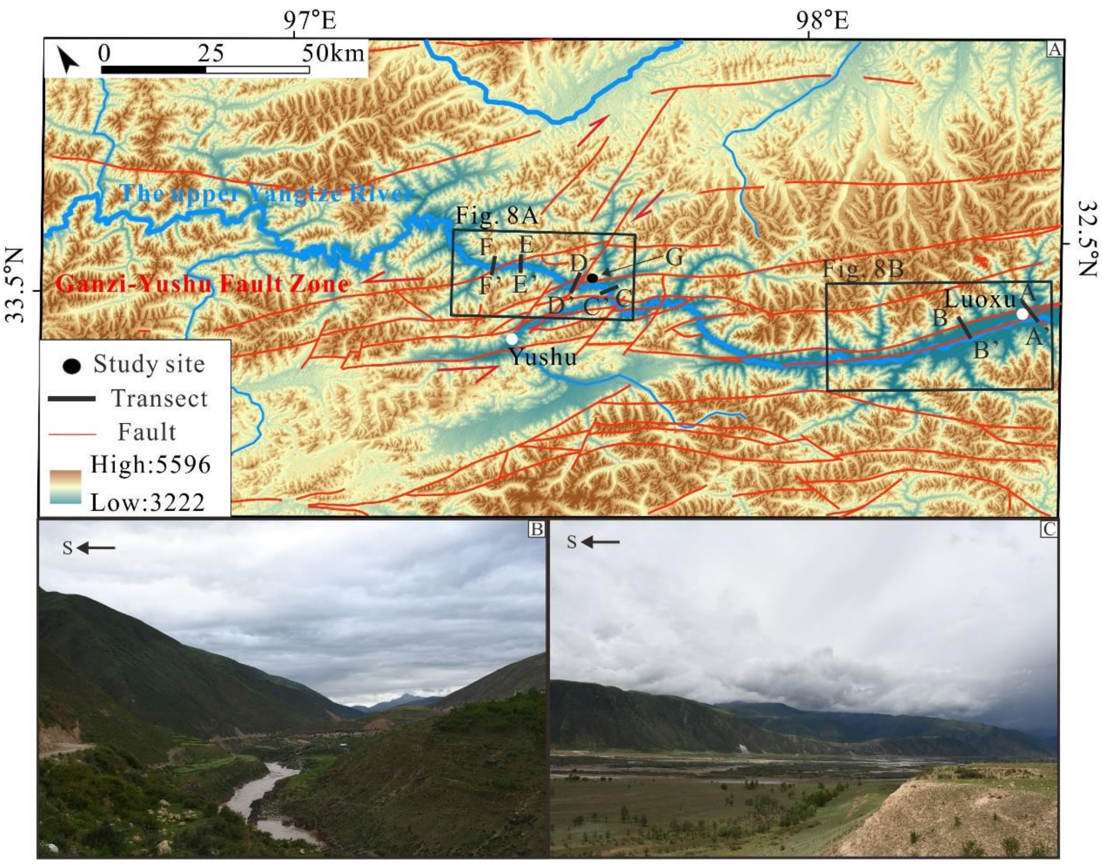

Figure 2. (A) Topographic map of the study area in the headwaters of the Yangtze River, ETP. Depicted faults are from the China Geological Archives (1:500000, http://www.ngac.org.cn/Map/List). The rectangles illustrate the areas with fluvial terraces in the Tongtian gorge and Luoxu basin, respectively. AA', BB', CC', DD', EE', FF' are seven studied transects in the upper Yangtze River catchment, G point is a site with typical interbedded fluvial, debris and colluvium deposits. (B) The landscape of the gorge with deep incision and slopes in bare bedrock in the Yushu area. (C) Basin landscape with wide valley and slope with thick soil in the Luoxu area.

The study area in the headwaters of the Yangtze River is situated in the alpine climate zone with strong winds and low temperature. The average annual temperature is below 0 °C. Currently, a mild and humid climate dominates the lower valley at the eastern edge of the Luoxu basin (Figure 2). The rainfall generally decreases from southeast to northwest, but increases significantly in the transitional area from the Luoxu basin to the Tongtian gorge because of the topographic effects (Figure 3A).

The average elevation of the study area is ~4,500 m. The northeastern part is flat with some wide glacial valleys, contrasting with the high relief with deep valleys and inter-montane basins which are due to intensive fluvial incision and the fault activities in the southwest (Figure 2). The headwaters of the Yangtze River flow over a distance of 350 km in the study area, and present steep channels in a detachment limited condition (Rhoads, 2020) in the uplifted region (Yushu) (Figure 2B) and graded channels in a transport limited condition (Rhoads, 2020) in the subsidence region (Luoxu) (Figure 2C). Because of the heterogeneous tectonic background, this area is dominated by a deep-canyon (e.g. Tongtian gorge) in the uplifted region and a wide valley in the rift basins (e.g. Luoxu basin) (Figure 3B) (Zhou et al., 2013). Two knickpoints are present along the Yangtze River in this region (Figure 3B).

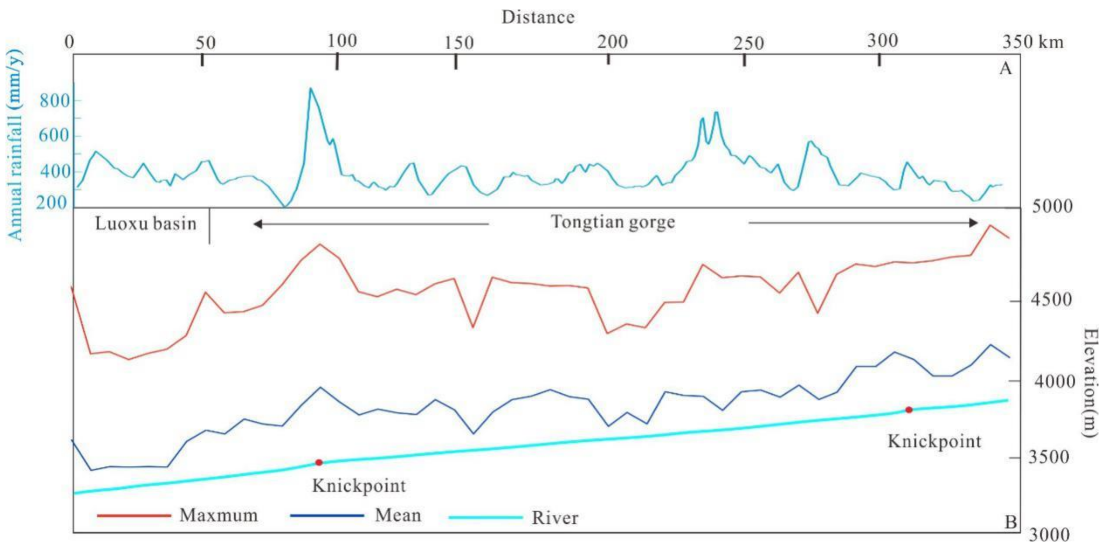

Figure 3. (A) The annual rainfall along the valley of the upper Yangtze River. (B) Maximum (red) and mean (blue) elevation of a swath profile (5 km×350 km) along the upper Yangtze River and the longitudinal profile of the Yangtze River (fluorescent-blue). Two knickpoints are present in this region.

3. Methods

3.1. Field Studies

River terraces have been well developed along the river valley in the headwaters of Yangtze River. Here, the terrace sequence was determined based on the height of a terrace surface above present floodplain (apf) and the spatially continuous extension of terrace outcrops. We mapped the sequence of fluvial terraces by the combination of field investigations and remote-sensing images.

Six geomorphic transects were selected as a representative of the suite of fluvial terraces. Two of those transects, AA' and BB' are located in the Luoxu basin (N32.55°-32.44°, E97.69°-98.03°), a tectonically relatively subsided block (Figure 2), while other transects CC' (at the site of Shaijingtai, N33.00°, E97.25°), DD'(at the site of Moluo, N33.00°, E97.21°), EE' (at the site of Zhongda, E97.11°, N33.14°) and FF' (at the site of Baliria, E97.06°, N33.17°) are distributed along the Tongtian gorge in a relatively uplifted block (Figure 2). The site G (Zhimenda, N33.00°, E97.24°) shows a typical sequence of inter-bedded fluvial sediments and mass-flow sediments such as debris flows (see discussion) (Figure 2). The terrace elevations were accurately measured using GPS with a maximum error of 5 m. Sedimentary structures were described according to the facies codes of Miall (1996).

3.2. OSL dating

The OSL samples were taken from different terraces (Table 2) by hammering a steel tube 25 cm long with a diameter of 5 cm into the sand layers of fresh sections. Pure quartz was extracted from the middle part of the tubes using common methods (30% H_2O_2, 10% HCl, wet sieving, 40% HF).

All the luminescence analyses were carried out on an automated Risø reader equipped with blue (470 nm; ~80 mW cm^2) LEDs and IR laser diode (870 nm, ~135 mW.cm^2). Quartz OSL signals were collected through a 7.5 mm Schott U-340 (UV) glass filter (emission 330±35 nm). The quartz equivalent doses (De) were measured using a standard single-aliquot regenerative dose (SAR) protocol (Murray and Wintle, 2000; 2003). Preheating of natural and regenerative doses was for 10 s at 240°C, and the response to the test dose was measured after a cut-heat to 200°C. Optical stimulation with the blue diodes was for 40 s at 125°C. The initial 0.16 s of the decay curve was used in the calculations, minus a background evaluated from the following 0.16~0.32s. After measurements of the response to the test dose, a high-temperature bleaching was performed by stimulating with the blue diodes for 40 s at 280°C (Murray and Wintle, 2003). For each aliquot, the dose response was obtained by measurements of the response to four regenerative doses. This was followed by three additional measurements to obtain estimates of recuperation and recycling (Murray and Wintle, 2000) and purity test (OSL IR depletion ratio; Duller, 2003). All the above laboratory measurements were carried out at the Luminescence dating Laboratory of Geomorphic Process team, the School of Geography and Ocean Science, Nanjing University.

The sediments at both ends of the tubes were used for water content and radioactive element analysis. The material (about 20 g) was first dried and then grounded to powder to determine concentrations of U, Th, and K using Inductively Coupled Plasma Mass Spectrometry (ICP-MS) and Inductively Coupled Plasma Optical Emission Spectrometry (ICP-OES) at the Geochemistry Laboratory of the School of Earth Sciences and Engineering, Nanjing University. Because the water content varied during the long-term burial period, we assumed 50% of the saturated water content as the average value during historical time with an uncertainty of 50% to this value to allow for possible fluctuations. Based on applying conversion factors from Guérin (Guérin and Adamiec, 2011) and beta attenuation factors from Mejdahl (Mejdahl, 1979), the external beta and gamma dose rate were calculated using the radionuclide concentration.

4. Results and Interpretation

4.1. Terraces in the relatively subsiding Luoxu basin

4.1.1. The AA' section

Three terraces correlate with T7, T4b and T1 (see terrace correlation below) in the transect AA' (Figures 2 and 4A). Gravels in all terrace deposits consist of quartzite, sandstone, granite, conglomerate and diabase. The sediment of T7 (62 m apf) was divided in three units from the bottom to the top (Figure 5C). The basal unit (36 m thick) is mainly composed of poorly sorted gravels and deposited as planar cross-bedded (Gp facies) and disorganized, clast-supported beds (Gcm facies) (Figure 5C). The base of the gravels is not exposed. The gravels are mainly rounded to sub-rounded, 10~20 cm in diameter. The middle unit (1.5 m thick) is fine sand with a massive structure (Sm facies). The top unit (0.5 m thick) is silt with small pebbles, showing a massive structure (Fm facies) (Figure 5C).

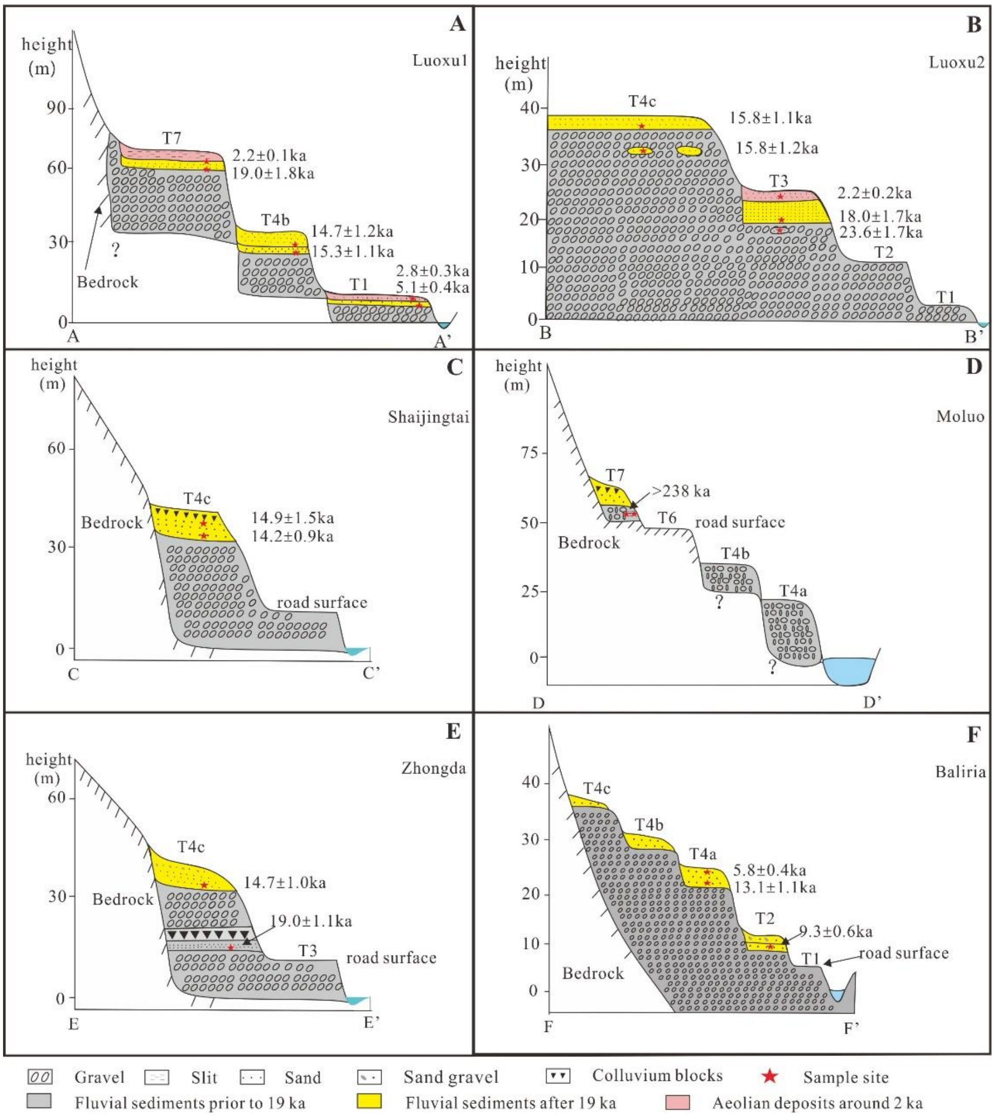

Figure 4. Schematic cross sections and ages along the studied geomorphic transects (see their locations in Fig.2). (A), (B), (C), (D), (E) and (F) are the terraces at transects AA', BB', CC', DD', EE', FF', respectively.

T4b is at 28 m apf in transect AA' (Figure 4A). We divide the sediment in two units from the bottom to the top (Figure 4 and 5D). The basal unit (1 m thick) consists of imbricated gravels with planar cross bedding (Gp facies) and occurs in organized, clast-supported beds (Gcm facies) (base not exposed) (Figure 5D). The gravels are mainly rounded, 10~20 cm in diameter. The top unit (1.6 m thick) is sand with small pebbles. The lower part of that upper unit is coarse sand with horizontal lamination (Sh facies), and the topmost part is fine sand with a massive structure (Sm facies) (Figure 5D).

The lowest terrace (T1) is at 5 m apf. We divide the sediments in three units (Figures 4A and 5E). The 5 m thick imbricated gravels make up the bottom unit without exposed base and are deposited as planar cross-bedded (Gp facies) and disorganized, clast-supported layers (Gcm facies). The grain sizes of the gravels decrease upward from 10~30 cm to 5~8 cm in diameter. The middle unit (0.5 m thick) is coarse-grained sand with horizontal lamination (Sh facies). The top unit (1.6 m thick) is reddish silt with a massive structure (Sm facies) (Figure 5E).

All the sediments of T7, T4b and T1 show channel deposition of rounded and imbricated gravels at the base, followed by overbank deposition (with laminated structure) and/or aeolian sedimentation (with massive structure). The disorganized and massive gravels in the Gcm facies indicate rapid deposition by high concentrated stream flow, while the planar cross-beds in facies Gp are interpreted as the foresets of transverse 2-D gravel bedforms (Miall, 1996; Einsele, 2000). The sand in Sh facies suggests deposition by planar bed flows in channels, or sheet flood in upper-flow regime, while the massive structure (Sm and Fm facies) is due to rapid deposition of sand from the suspended load of waning flows in overbank or abandoned channels (Miall, 1996; Einsele, 2000).

4.1.2. The BB' section

Four terraces in transect BB' correlate with T4c, T3, T2 and T1 (see terrace correlation below) (Figures 2 and 4B). Gravel composition is similar in all terrace deposits, dominated by sandstone, granite, conglomerate, diabase, quartzite. T4c at 34 m apf contains two units (Figure 5F). The basal unit (4 m thick) is composed of imbricated gravels, deposited in horizontal beds (Gh facies) with some sand lenses, and organized in clast-supported beds (Gcm facies) (Figure 5F). The base of this unit is not exposed. The gravels are rounded with upward decreasing size from 10~20 cm to 5 cm diameter. The top unit (2.5 m thick) is sand with some pebbles, showing horizontal lamination (Sh facies).

Figure 5. (A) and (B) are the distributions of terraces at transect AA' in Luoxu 1 and transect BB' in Luoxu 2. (C), (D), (E), (F) are the sedimentary structure of sediments at terrace T7, T4b, T1, T4c in the Luoxu Basin. Fm-massive silt, Sm-massive sand, Sh- horizontal laminated sand, Gh-horizontal gravels, Gp-gravels with planar cross bedding, Gcm-clast supported gravels. The dashed line marks the boundary between different units.

The T3 surface is underlain by a lower 18 m thick gravel layer and an upper 2.5 m thick bed of fine sand with small pebbles. The structure of the gravel unit is planar-cross bedded (Gp facies) with some sand lenses, and occurring in disorganized, clast-supported and matrix-supported beds (Gcm and Gmm facies). The base of this unit is not exposed. The gravels are rounded, 30~50 cm and 10~20 cm in diameter. The top unit (2.5 m thick) is mainly consisting of sand with some pebbles. The lower part of this unit shows horizontal lamination (Sh facies), while the upper part is a fine silt with massive structure (Fm facies).

T2 and T1 extend at 13 m and 2 m apf along the river, respectively. All the units consist of imbricated gravels deposits with planar-cross bedding (Gp facies) and are organized in clast-supported beds (Gcm facies). The gravels are round, 20~30 cm in diameter. In contrast to the higher terraces, no fine-grained sediment covers the gravels of these terraces.

The gravels of the terraces in transect BB' were deposited by channel traction flow as indicated by the rounded shape and the imbricated traction structures (e.g. Gp facies). The sedimentary structures of all outcrops are similar to those in transect AA', indicating similar sedimentary processes and environments.

4.2. Terraces from the gorges in relatively uplifted segments

4.2.1. The CC' section

One terrace, T4c (see terrace correlation below), is identified in this section (Figures 2 and 4C) at Shaijingtai (SJT; N33.00°, E97.25°) at 34 m apf. It contains gravels, sand and angular blocks from the bottom to the top (Figure 4). We divided the sequence in three units according to the particle size and structural characteristics of the sediments. The lowest unit is dominated by imbricated gravels, deposited as planar-cross (Gp facies) and clast-supported beds (Gcm facies). The base of this unit is not exposed. The gravels are sub-rounded to rounded, 20~40 cm in diameter, and consist of diabase, sandstone, conglomerate, and granite. The middle unit (2.3 m thick) is composed of sand in its lower part and silty sand in its upper part. The sand deposit shows mainly horizontal lamination (Sh facies) with occasional small ripples (Sr facies) and massive structure (Sm facies). The silty sand shows also small ripple structures (Fl facies). The top unit is composed of chaotically structured, angular boulders (grey-green breccia, 10~15 cm in diameter).

The structure of sediments in transect CC’ shows a fluvial origin, covered with some sediments of mass-flow origin. Again, the poorly sorted, sub-rounded to round gravels in the Gcm facies indicate rapid aggradation as a channel lag, while the planar-cross beds (Gp facies) represent the foresets of low bars and dunes. The sand layers with horizontal lamination, cross bedding and massive structure show an upward decrease from coarse sand to fine sand, meaning a decline of transport energy. The small ripple (Fl facies) in silt indicates abandoned channel fills, while the chaotically angular gravels with oversized blocks are interpreted as debris flow sediments or landslide sediments.

4.2.2. The DD’ section

Four terraces correlate with T7, T6, T4b and T4a (see terrace correlation below) (Figures 2 and 4D). T7 at 55 m apf, is poorly preserved along the northern bank of the Yangtze River in the site of Moluo (ML) (N33.00°, E97.21°) (Figures 4 and 6B). The sediment sequence in that terrace comprises three units (Figure 6B). The lowest unit 1 (5 m thick) is composed of imbricated gravels with inter-fingering sand lenses. Towards the base the gravels are rounded to subrounded, 10~50 cm in diameter, deposited as planar-cross beds (Gp facies), and clast-supported (Gcm facies) (Figure 6B). Towards the top of unit 1 the gravels are angular to sub-angular, 5~15 cm in diameter, and matrix-supported (Gmm facies) (Figure 6B). All the gravels are composed of sandstone, diabase, granodiorite, quartzite, conglomerate and limestone. Unit 2 (3 m thick) in the middle part of the section is composed of sand layers with horizontally laminated structure (Sh facies). Some centimeter-scale angular pebbles are present inside the sand layer. The top unit 3 is consisting of disorganized grey-green angular blocks, 40~50 cm in diameter.

T6 at 42~46 m apf shows multiple cycles of channels, debris and colluvial sediments. The base of this sediment sequence is not exposed. T4b and T4a extend along the steep slope with disorganized structure of gravel (Figure 4). Because of the deep incision with steep slope, it was impossible to sample the sections and to describe the sedimentary structure in detail.

The sedimentary structures of Gp, Gcm, and Sh facies with imbricated gravels, rounded and sub-rounded gravels in the layers of T7, shows stream channel flow (Miall, 1996). In contrast, the disorganized angular gravels and matrix-supported gravels layers in unit 3 and the upper part of unit 1 suggest debris flow sediments or sediments due to mass wasting process from the hillslope (e.g. Hewitt et al., 2008).

4.2.3. The EE' section

Two terraces correlate with T4c and T3 in Zhongda (ZD; E97.11°, N33.14°) (Figures 2 and 4E) (see terrace correlation below). The gravels are composed of sandstone, diabase, granodiorite, quartzite, conglomerate and limestone. T4c and T3 occur at 34 m and 18 m apf, respectively (Figure 4). The sedimentary sequence of T4c is subdivided in four units (Figures 4 and 6C, D). The lowest unit 1 (3 m thick) is a horizontally laminated sand layer that contains several thin layers of angular small pebbles (Figure 6C). The overlying unit 2 (5 m thick) is composed of disorganized blocks (Figure 6C) which are angular with upward increasing size diameter (centimeter- to meter-scale; Figure 6C). A 4-m-thick gravel layer (unit 3) covers unit 2. It shows an imbrication structure, with planar-cross bedding and clast-supported beds (Gp and Gcm facies) (Figures 6C, D). The gravels are sub-angular to sub-rounded, 20~30 cm in diameter. Unit 4 (5 m thick) is composed of sand with some centimeter-scale pebbles in the upper part, showing a horizontally laminated structure (Sh facies) (Figure 6D).

T3 is composed of gravels with unexposed base, on which a road was constructed without outcrop. The structure of disorganized gravels with appearance of oversized blocks (unit 1 and the bottom of unit 2) in T4c sediment sequence shows a debris flow origin (e.g. Li et al., 2018) (Figure 6C). The multiple cycles of alternating fluvial sands with their typical characteristics and angular debris blocks within unit 1 of the T4c sediment sequence indicates a process of rapid succession of fluvial and mass-wasting origin. This may be an expression of the frequent interruption of the fluvial process (imbricated rounded gravels in Gp and Gcm facies of unit 3 in T4c sediments) by the supply of large angular debris from small tributaries and hillsides in the form of alluvial cones or debris slopes. Lateral erosion of the river in the gorge resulted in sporadic bedrock exposure along the hillslope.

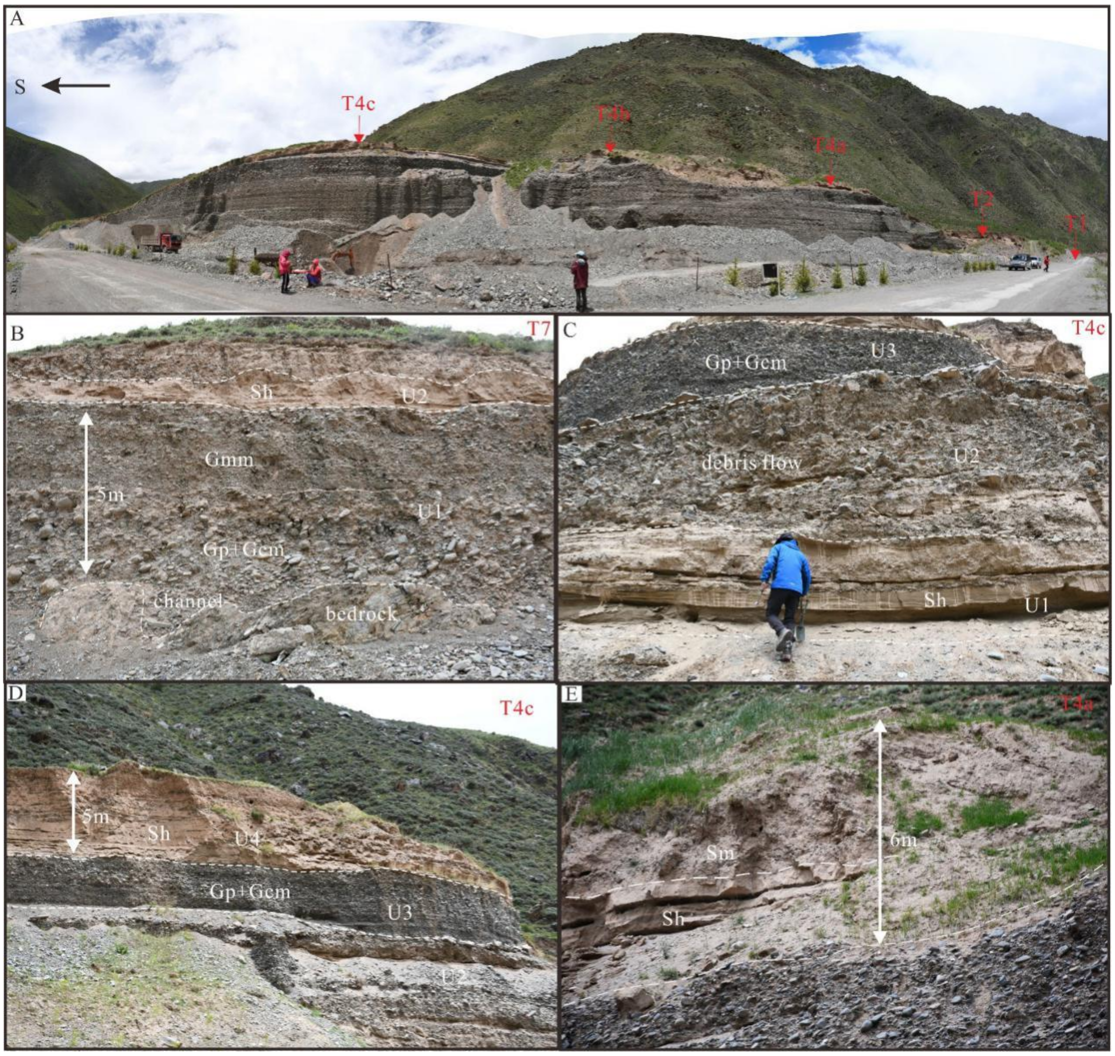

Figure 6. Terraces and sediments in the Tongtian gorge. (A) the terraces at the transect FF’. (B) the sedimentary profile of T7 in transect DD’. (C) and (D) the sedimentary profiles of T4c in transect EE’. (E) the sedimentary profile of T4a in transect FF’. Sm-massive sand, Sh-horizontal laminated sand, Gp-planar cross bedding gravel, Gcm-clast-supported gravel beds, Gmm-matrix-supported gravel beds. The dashed line marks the boundary between units.

4.2.4. The FF’ section

In contrast to the sections described above, the gravels of transect of FF' (see location in Figures 2 and 4) accumulated in a 33 m thick layer. They were incised to form five terraces, T4c, T4b, T4a, T2, T1, at 33, 28, 22, 12, 5~6 m apf, in Baliria (BLRA; E97.06°, N33.17°), respectively (Figures 4 and 6A). The composition of gravels is similar to that in the previous transects. The gravels show imbrication, planar-cross bedding (Gp facies) and are clast-supported (Gcm facies), 20~30 cm in diameter. The base of the sediment sequence is not exposed.

T4c and T4b are covered with sand, but the outcrop, as a cliff, was not accessible for description of the sedimentary characteristics.

T4a has two sediment units covering the underlying gravel fillings. The lower unit1 (4 m thick) is composed of sand with horizontally laminated beds (Sh facies) (Figure 6E). The upper unit 2 (2 m thick) is a massive sand bed (Sm facies) with pebbles (Figure 6E).

The sediment of T2 shows two units covering the underlying gravels. The lower unit 1 (1.5 m thick) is a sand layer with small ripple cross-lamination (Sr facies) in the lower part and horizontal laminated structure (Sh facies) in the upper part. The upper unit 2 (2 m thick) is a massive sand (Sm facies) layer with centimeter-scale pebbles. T1 is located on the road surface without outcrop.

The gravels and sands in this cut-in-fill terraces show thick fluvial sediments. The lower gravels with Gcm and Gp facies and the upper cross-laminated, horizontally laminated and massive sands (Sr, Sh, Sm facies) point to variable energy in the fluvial sediments.

4.3. A typical sequence of alternating fluvial and mass waste sedimentation

The interbedded fluvial, debris and colluvium deposits are widespread in the gorge; one typical sequence was described at the site of Zhimengda (ZMD, N33.00°, E97.24°) (site G in Figure 2). The structure of the sedimentary section ZMD shows a sequence of alternating layers of rounded gravels, sands and angular gravels and boulders, which may indicate alternating phases of fluvial and debris or colluvium deposition (Figure

7). The top of the sediment sequence is ~53 m apf, which correlates with T7. The upper ~30 m sediments may be subdivided in eleven units (Figure 7 A). From bottom to top, unit 1 (5 m thick) is composed of disorganized breccia, 5~10 cm in diameter. Unit 2 (1 m thick) is composed of sand with horizontally laminated structure (Sh facies). Unit 3 (1 m thick) contains imbricated gravels with planar cross-bedding, and clast-supported beds (Gcm facies). The gravels are rounded, 10~20 cm in diameter, and consist of sandstone, diabase, quartz, conglomerate and limestone. Unit 4 (2 m thick) is a horizontally laminated, fine-grained sand bed (Sh facies). Unit 5 (7.5 m thick) is composed of rounded gravels with planar cross bedding (Gp facies), trough cross-bedding (Gt facies) and clast-supported beds (Gcm facies), containing three layers of angular boulders (0.5-1m in diameter). Unit 6 (1.5 m thick) is composed of sand with planar cross-bedding (Sp), horizontal lamination (Sh) and ripple cross-bedding (Sr) from bottom to top. Unit 7 (7 m thick) is composed of rounded gravels (5-10 cm in diameter) with planar cross-bedding (Gp facies) and gravel sheets with imbrication. The 1.5 m thick coarse sand layer of unit 8 is a deposit with planar cross-bedding (Sp facies) containing some angular pebbles (~1 cm in diameter). The overlying unit 9 (0.8 m thick) is a breccia (pebbles are 1-3 cm in diameter) with crude imbrication containing sand lenses with planar cross-bedded structure (Sp facies). Unit 10 (0.5 m thick) is composed of horizontally laminated, silty sand (Fl facies) and sand (Sh facies). The topmost unit 11 (1 m thick) is consisting of angular gravels (2-6 cm in diameter) contained in a silt matrix.

The disorganized breccia in units 1 and 9 and the angular boulders in unit 5 are interpreted as debris flow or colluvium deposits. The rounded and sub-rounded gravels and sand with imbrication structures, planar or trough cross-bedding, horizontal lamination and ripples in other units indicate a fluvial origin. The interbedded deposition of fluvial and debris and colluvium sediments points to a striking change in deposition conditions and provenance (e.g., Gao et al., 2018). They are the expression of the interplay between fluvial processes and mass-wasting events that characterizes the evolution in the gorge.

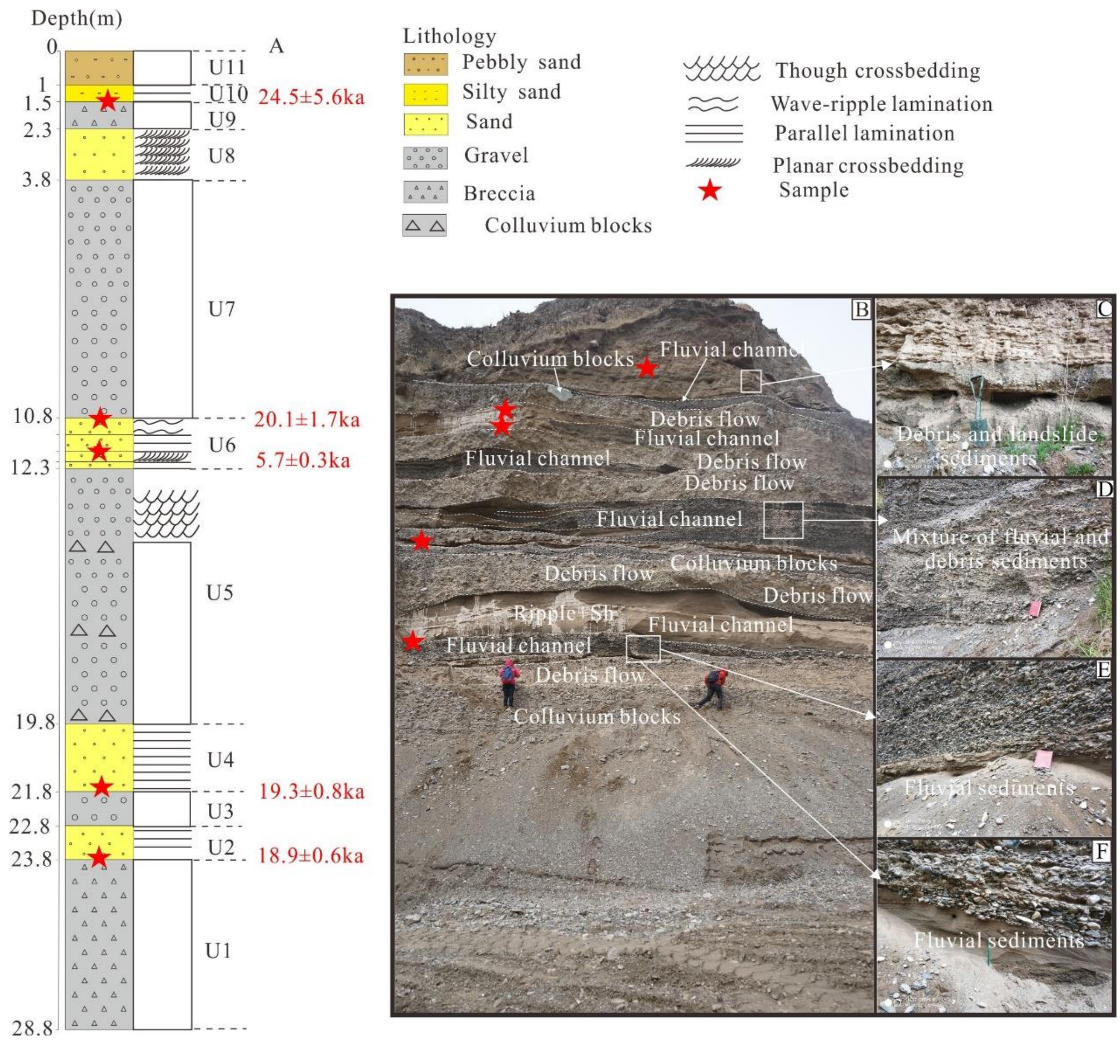

Figure 7. (A) Stratigraphic column, OSL ages and location of samples at ZMD (units 1-11). (B) Typical sediments with alternating fluvial, debris and colluvium beds at the ZMD site. White dashed line marks the boundary between units. (C-D) Mixture of fluvial and debris-flow sediments in Fig. 7B. (E) and (F) are fluvial sediments in Fig. 7B.

4.4. OSL ages

The luminescence decay curves (Figures 8A and C) show a rapid decrease, implying dominance of a fast component. The dose response curves are well-fitted with a single saturating exponential function (Figures 8A and C). The histograms of the equivalent dose from the samples such as LX-E-OSL-220 and LX-E-OSL-100, show a normal distribution (Figures 8B and D), indicating that the quartz is compatible with a well-bleached nature and the chronologic result is reliable. Table 1 summarizes the analytical data and OSL ages.

Table 1

Summary of sample code; U, Th, and K concentrations; estimates of past water content (W.C.); dose rates; equivalent doses (De); overdispersion and age for fluvial sediments for headwaters of the Yangtze River, China.

Field code	Grain size	Depth(m)	U (ppm)	Th (ppm)	K (%)	W.C (%)	Dose rate(Gy/ka)	De(Gy)	OD(%)	Age(ka)
LX-OSL-110	63-90	1.1	1.43±0.07	7.44±0.37	1.26±0.06	14±7	2.32±0.35	6.6±0.6	28±7	2.8±0.3
LX-OSL-210	63-90	2.1	1.15±0.06	5.43±0.27	1.19±0.06	16±8	2.06±0.3	10.5±0.7	19±4	5.1±0.4
LX-B-OSL-100	63-90	1	2.31±0.12	10.79±0.54	1.67±0.08	26±13	2.79±0.39	41.0±1.5	9±3	14.7±1.2
LX-B-OSL-150	63-90	1.5	1.63±0.08	7.02±0.35	1.19±0.06	15±8	2.26±0.34	34.6±1.7	12±4	15.3±1.1
LX-C-OSL-60	63-90	0.6	2.26±0.11	11.16±0.56	1.56±0.08	17±8	2.93±0.45	6.4±0.2	4±2	2.2±0.1
LX-C-OSL-160	63-90	1.6	2.43±0.12	9.72±0.49	1.44±0.07	32±16	2.46±0.32	46.9±2.0	10±4	19.0±1.8
LX-D-OSL200	63-90	2	2.00±0.10	8.69±0.43	1.36±0.07	18±9	2.54±0.38	40.2±1.5	8±3	15.8±1.1
LX-D-OSL450	63-90	4.5	1.36±0.07	6.57±0.33	1.27±0.06	13±7	2.25±0.34	35.6±2.1	9±6	15.8±1.2
LX-E-OSL-100	63-90	1	2.06±0.10	11.38±0.57	1.74±0.09	21±10	2.95±0.44	6.6±0.2	6±2	2.2±0.2
LX-E-OSL-220	63-90	2.2	2.11±0.11	11.18±0.56	1.74±0.09	34±17	2.66±0.35	48.0±1.5	7±3	18.0±1.7
LX-E-OSL-650	63-150	6.5	1.29±0.06	6.71±0.34	1.38±0.07	16±8	2.30±0.34	54.2±3.0	17±6	23.6±1.7
SJT-OSL-1	63-90	4	1.59±0.08	8.16±0.41	1.49±0.07	35±17	2.26±0.68	42.3±1.7	7±3	14.9±1.5
SJY-OSL-2	63-90	5.5	1.41±0.07	7.10±0.35	1.28±0.06	13±7	2.36±0.36	33.5±1.3	7±5	14.2±0.9
ZD-OSL-1	63-90	5	2.18±0.11	8.74±0.44	1.44±0.07	17±8	2.69±0.40	39.5±1.4	8±4	14.7±1.0
ZD-OSL-2	63-90	37	1.94±0.10	10.46±0.52	1.54±0.07	12±6	2.94±0.47	55.9±1.7	3±6	19.0±1.1
BLRA-OSL-1	63-90	3	1.12±0.06	5.52±0.28	1.00±0.05	15±8	1.93±0.27	11.3±0.6	16±4	5.8±0.4
BLRA-OSL-2	63-90	5	1.42±0.07	6.55±0.33	1.17±0.06	16±8	2.20±0.32	28.8±1.9	16±5	13.1±1.1
BLRA-OSL-3	63-90	2	1.33±0.07	6.72±0.34	1.21±0.06	11±5	2.32±0.36	21.5±1.0	12±3	9.3±0.6
ML-OSL-2	90-150	6.5	1.19±0.06	7.64±0.38	1.37±0.07	14±7	2.39±0.36	570.3±64.9	23±10	238.2±30.0
ZMD-A-OSL-1	63-90	1.5	2.27±0.11	11.11±0.56	2.21±0.11	20±10	3.41±0.53	83.6	29±10	24.5±5.6
ZMD-A-OSL-2	90-150	11.5	1.53±0.08	7.78±0.39	1.61±0.08	23±11	2.48±0.35	49.8±2.2	9±4	20.1±1.7
ZMD-A-OSL-3	63-90	12	1.32±0.07	6.95±0.35	1.38±0.07	16±8	2.35±0.35	13.5±0.2	4±2	5.7±0.3
ZMD-1	63-90	30	2.03±0.10	9.92±0.50	1.44±0.03	0.6±0.3	2.67±0.58	51.5±1.9	6±3	19.3±0.8
ZMD-2	63-90	35	2.13±0.11	10.88±0.54	1.59±0.03	1.2±0.6	2.87±0.61	54.5±1.6	4±4	18.9±0.6

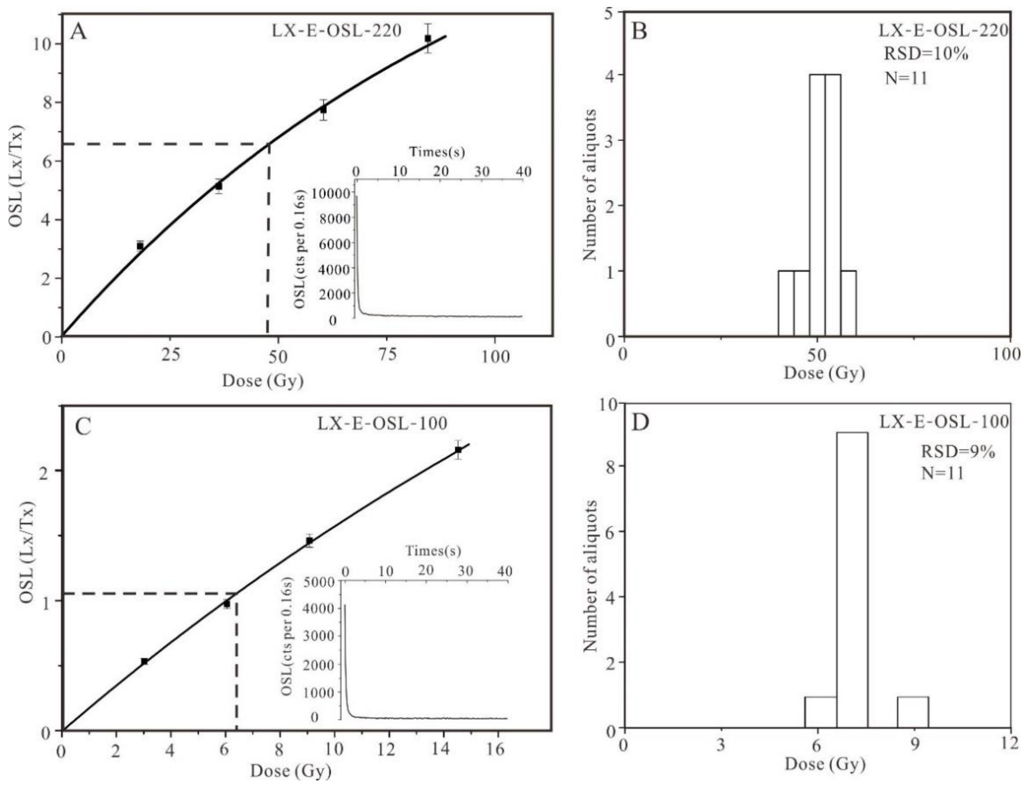

Figure 8. (A) and (C) are dose response curves for aliquots of samples LX-E-OSL-220 and LX-E-OSL-100 with inset figures showing the natural decay curves. (B) and (D) are histogram of De distribution of the samples LX-E-OSL-220 and LX-E-OSL-100.

OSL dating results of fluvial, debris and colluvium deposits in this region yield 25 ages ranging from 2.2 ka to 24.5 ka, except the sample ML-OSL-2 (Table 1). In the subsidence region (Luoxu basin), T7, T4c, T4b, T3, are dated around 14-19 ka within the error margins, and T1 at c. 5 ka (Table 2 and Figure 4). The sand lens from the accumulation series below T3 is dated around 24 ka, which indicates the 62 m thick fluvial sediments accumulated prior to 24 ka. The samples from the massive silty layers of top units with ages of 2.2 ka in T7, 2.8 ka in T4b and 2.2 ka in T3 reflect reworked aeolian sediments covering these terraces (Figure 4).

In the uplifted region (Tongtian gorge), the terraces T4c and T4a are dated around 12-17 ka, and T2 at c. 9 ka (Table 2; Figure 4). The sand lens in site ZD is dated at 19 ka and demonstrates debris-flow sediment (T4c in transect EE') were deposited during the period 14.7-19.0 ka (Figure 6C).The sand lens in the sediment sequence of ML is dated >238 ka, indicating former aggradation before 238 ka (Figure 6B).

According to the definition of terrace ages (Vandenberghe, 2015), the age of a terrace is defined as the age of abandonment of the channels on their floodplain before incision, in other words lithologically corresponding with the boundary between gravel deposits and fine-grained floodplain deposits. It means that in this study the terrace age is just after the youngest age in the gravels (Table 2). The valley in the headwaters of the Yangtze River has been filled with c. 60 m thick sediments before 19 ka. Subsequently, the river transformed from aggradation to generally continuous incision, episodically interrupted by phases of stability or lateral erosion. The latter interruptions initiated the formation of terraces at 62-38 m (T7-T5), 35-18 m (T4-T3), 13-11 m (T2), and 5 m (T1) above present floodplain, with ages of ~19 ka, ~17-13 ka , ~9 ka, and ~5 ka, respectively (Table 2).

As for the interbedded deposition of fluvial, debris and colluvium sediments in ZMD, the OSL ages of units 2, 4, 6, 10 center around 20 ka, except the age of 5.7 ka of unit 6 (Figure7). Thus, the interaction between fluvial, debris flow and colluvium processes happened around 20 ka. The age of 5.7 ka is to be considered as an outlier and should be disregarded.

4.5. Correlation of the terraces

Seven terraces were mapped along the river (labelled as T1 to T7 from young to old) (Figure 4 and Table 2). They are correlated on the base of elevation above the floodplain and age of deposits. In the Luoxu basin, they are typified by the shape of the wide valley and the low gradient of the riverbed, show similar sedimentary properties: fluvial gravels of various thickness are interbedded with sand lenses, silts, and ultimately capped by pebbly sand (Figure 6). In contrast, the gorge area (i.e. Yushu area) is characterized by its narrow transversal profile and steep valley sides, while the boulders and breccia between fluvial gravels and sands in the gorge terraces illustrate a provenance from the hillside or small tributaries (Figure 5). Terraces in the gorge, for example at Baliria, are relatively narrow and spatially discontinuous (Figures 6A and 9A), but they are wide and flat in the Luoxu basin (Figures 5A, B and 9B).

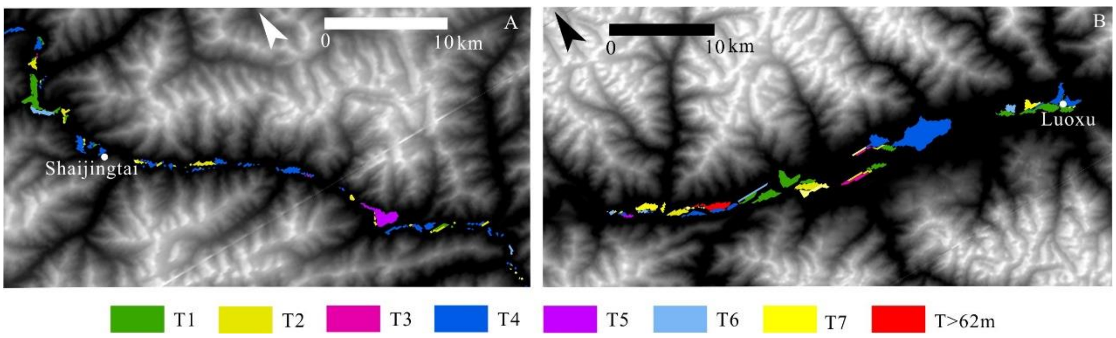

Figure 9. Terrace distribution in the Tongtian gorge (A) and the Luoxu Basin (B) (see locations in Fig.2). Arrows show north direction.

Table 2

The elevations apf, ages and incision rates (elevation/age) after terrace formation in the Luoxu basin and Tongtian gorge (headwaters of the Yangtze River, ETP).

Terrace sequence	Luoxu basin apf (m)	Luoxu basin Terrace age (ka)	Luoxu basin Incision rate (mm/yr)	Tongtian gorge apf (m)	Tongtian gorge Terrace age (ka)	Tongtian gorge Incision rate (mm/yr)
T7	62	19.0±1.8	<3.3	55		
T6				42-46		
T5				38		
T4c	35	15.8±1.1	2.2	34	17-13	2-2.6
T4b	28	15.3±1.1	1.8			
T4a				22	13.1±1.1	1.7
T3	18	<18.0±1.7		18		
T2	13			11	9.3±0.6	1.2
T1	5	5.1±0.4	1.0	5		

5. Discussion

5.1. Response of terrace morphology to tectonic activities

Heterogeneous tectonic activities may result in relative uplift and subsidence, leading to different patterns of fluvial sedimentation and valley evolution in different parts of the drainage system (Whipple et al., 1999; Bridgland et al., 2008; Vandenberghe et al., 2011; Wang et al., 2014; Duvall et al., 2015). Indeed, the diverse tectonic activities in one catchment could cause considerable changes of local channel slope, which may lead to local changes in stream transport capacity and further fluvial responses in different tectonic blocks of the catchment. For example, the Huangshui River (NE Tibetan Plateau) incised and an erosion terrace developed in the uplifted areas (creating deep gorges), and meanwhile thick deposits formed an accumulation terrace in the subsiding areas (Wang et al., 2010, 2014; Vandenberghe et al., 2011).

In contrast to such a succession, the headwaters of the Yangtze River show similar sedimentary processes (a single thick valley filling followed by continuous incision) and terrace patterns (cut-in-fill terrace) both in the relatively uplifted (Tongtian gorge) and subsiding (Luoxu basin) areas during the late Quaternary (Figure 10). Compared to the Huangshui River catchment, the headwaters of the Yangtze River occur at higher altitude and are characterized by stronger freeze-thaw processes, especially during the last ice age (Heyman et al., 2011; Ou et al., 2013), high relief and frequent slope failures

(Korup et al., 2010). Large amounts of sediments supplied to the valleys in the headwaters of the Yangtze River during the LGM, may have resulted in the transition from detachment-limited to transport-limited conditions of the drainage system, and extremely thick valley aggradation at the maximum cold conditions during the last glacial maximum (LGM). This exclusive aggradation may have restrained the effects of changing local valley slopes in the catchment caused by relative tectonic uplift and subsidence. In addition, similar incision rates in both uplifted and subsided areas reflect the negligible effects of tectonic movements on the terrace formation (Table 2). Thus, if tectonic differentiation between the basins and uplifted regions may be excluded as a cause for the different kinds of terrace formation, we suggest that the immense amount of sediment input into the drainage system may be the primary steering factor for fluvial reaction.

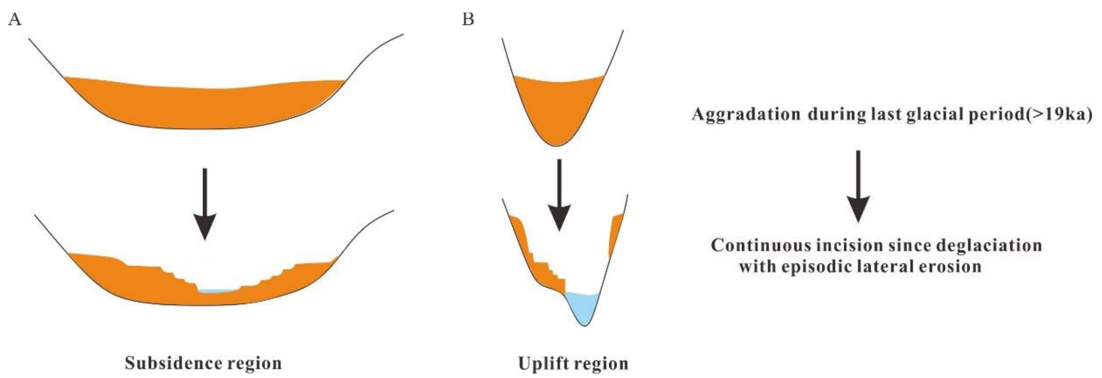

Figure 10. Conceptual model of different terrace morphology with mainly accumulation in the relatively subsided basins (Luoxu basin) (A) and formation of gorges in the relatively uplifted regions (Tongtian gorge) (B) in the headwaters of the Yangtze River during the late Quaternary.

In spite of the similar terrace pattern and sedimentary processes in the subsided and uplifted areas, the spatial distribution and morphological outlook of the terraces are different in the individual tectonic blocks. The subsided area, the Luoxu basin, provides large storage space for lateral channel erosion and is characterized by wide and flat terraces in the center of the valley (Figure 10A). In contrast, in the uplifted region, spaces are limited for lateral erosion, and narrow terraces extend stepwise along the valley sides. In the gorge, bedrock is sometimes exposed in spite of the cut-in-fill terrace style (Figure 10B). This observation confirms that the uplift causes mainly downward erosion without terraces or with only narrow terraces along the river channel, while lateral erosion contributes to the formation of wide terraces in the case of subsidence (e.g. Wang et al., 2015; Bender et al, 2016, 2019).

5.2. Response of terrace formation to climate change

During LGM, low temperature and humidity and weak monsoon activity (Figures 11 C and D) were favorable for low vegetation density (Zhao et al., 2020) and strong freeze-thaw processes, which induced frequent and extreme mass movement and even glacial processes in the east Tibetan Plateau (Ou et al., 2013; Heyman et al., 2011). Those processes resulted in the supply of large amounts of sediments to the river channels and thick valley aggradation. This aggradation phase is consistent with fluvial aggradation around the Tibet Plateau during the last glacial periods (e.g. Ray and Srivastava., 2010; Vandenberghe et al., 2011; Kothyari et al., 2016; Chahal et al., 2019). During the phase of deglaciation, monsoon activity became stronger with increased precipitation and denser vegetation cover (Figures 11 C and D). This resulted in higher discharges and reduced sediment input, causing river incision and stepped terrace formation from c. 19 to 11 ka. Thus, episodic weak aggradation resumed during the phase of general river degradation after 19 ka, developing terraces T6 to T3 (Figure11). After that, temperature increased with small fluctuations while monsoon precipitation remained relatively stable (Figure 11). As a result vegetation recovered steadily (Zhao et al., 2020), leading to continued incision. Small fluctuations of precipitation and temperature during the Holocene (Figure 11), and related changes of vegetation cover (Zhao et al., 2020), may have resulted in episodic interruptions of the general incision and the formation of terraces T2 and T1 at 9 ka and 5 ka, respectively (Figure 11C). However, internal dynamic factors or episodic tectonic movements cannot be excluded for these Holocene terrace formations (Schumm, 1993).

Fluvial aggradation during the cold LGM and incision during the next deglacial phase occur widely in the surrounding areas. The Lancang River near the study area experienced aggradation at 25-15 ka and incised afterwards (Zhang et al., 2018). In the Himalaya, dry climate conditions during cold periods led to valley filling, while rivers incised and formed terraces at wetter episodes during the late Quaternary (Ray and Srivastava, 2010). In addition, in the Central Kumaun Himalaya, the major phase of Saryu River valley filling was dated with the results between 22 and 14 ka (Kothyari et al, 2016). The Zanskar valley (NW Himalaya) aggraded during the climatic transition from the dry LGM to the wet early Holocene (20-12 ka) and followed by rapid incision due to the strong India Monsoon (Chahal et al., 2019). The effective moisture availability in the Asia monsoon edge was relatively low during LGM and high during the Holocene (Figure 11B). Thus, we hypothesize that the glaciation and freezing processes during the LGM in high mountains could provide plenty of sediments to the valley. But, melting of glacier ice (Heyman et al., 2011) and intensified monsoon precipitation since deglaciation (Zhao et al., 2020) might contribute to increased river discharge and river incision in this high relief area.

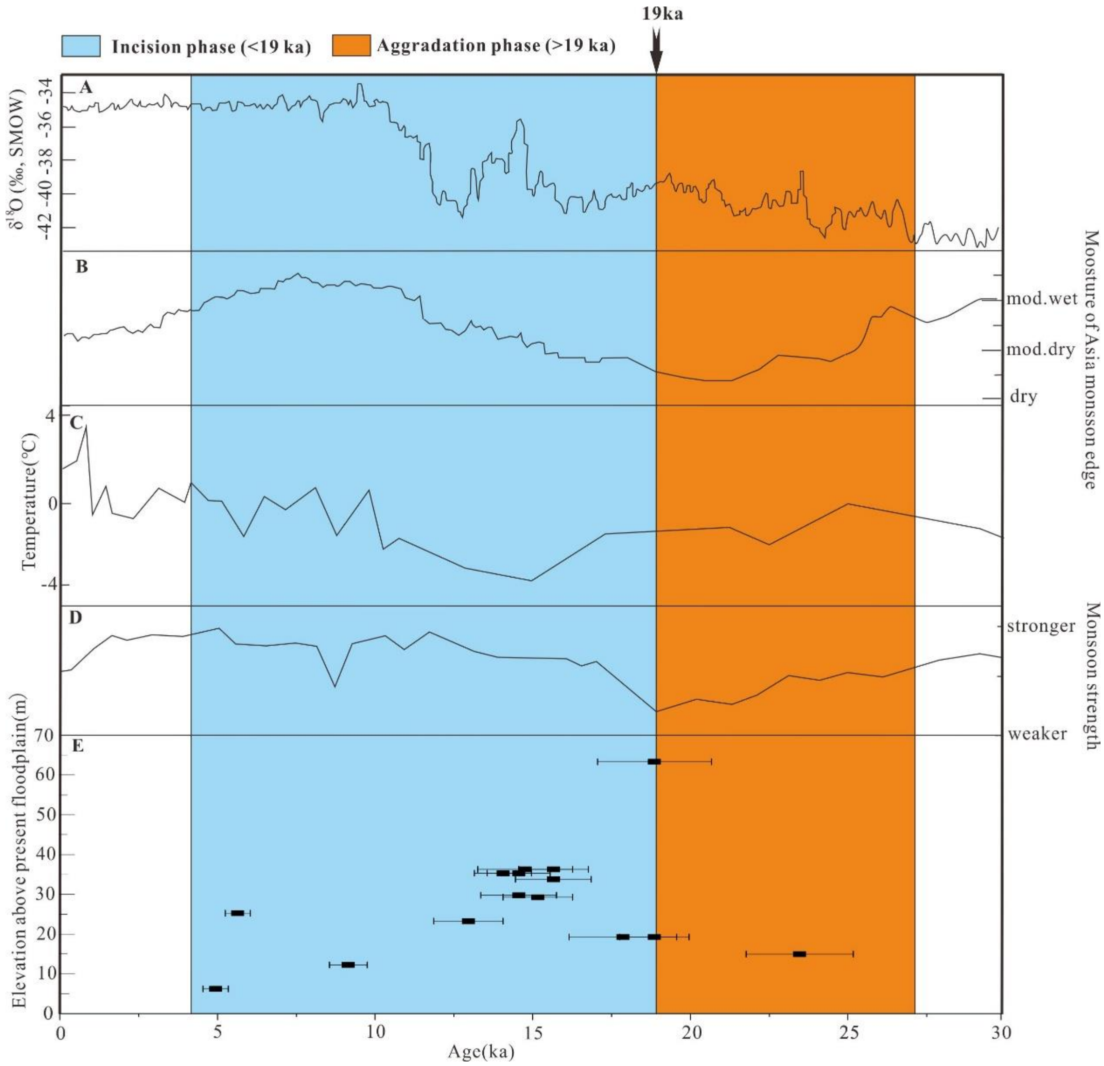

Figure 11. (A) Oxygen isotope records from the Greenland ice sheet (GRIP) (Johnsen et al., 2001). (B) The mean effective moisture from the Asian monsoon edge (Berger and Loutre, 1991). (C) and (D) are mean annul temperature and monsoon strength in Zoige basin in the ETP (Zhao et al., 2020). (E) OSL- ages of valley fill vs. elevation apf for fluvial terraces in this study.

5.3. The potential effects of extreme events in the fluvial evolution of the upper Yangtze River

The fact that mass-flow and slope deposits did not occur continuously in the sections but rather episodically, especially in the gorge terraces and in the ZMD section, points to occasional interruption of the fluvial process. In addition, the spatially irregular occurrence of thick gravel deposits of >19 ka age (Figure 4) points to the local presence of mass-flow and slope processes. Therefore, it is suggested that the latter deposits may be attributed to local occurrence of slope failures or alluvial fans. Considering the combined evidence of local and temporary presence of those deposits suggests local and temporary favorable conditions to initiate this kind of slope processes, it means rather exceptional or extreme conditions.

In the headwaters of the Yangtze River, the rugged terrain with frequent fault activities is episodically vulnerable to extreme mass wasting and strong local orographic precipitation, which may lead to extreme geomorphological processes such as landslides and debris flows (e.g. Bao et al., 2020). This chain of successive extreme events has produced abundant sediments to the valleys, and resulted in the repeatedly short time blocking of the channel (such as the landslides in Baiyu in October 2018; e.g. Liu et al., 2020), recorded as episodic debris and slope deposit interbedded in the fluvial sediment sequence around 20 ka at the site of the ZMD site in the gorge area.

The multiple cycles of fluvial, debris flows and colluvium layers around 20 ka at the sites of ZD and ZMD indicate that the change from cold-dry to warm-wet (Figure 11) at c. 20 ka in combination with the delayed re-vegetation of the hillslopes (e.g. Sewell et al., 2015), may have promoted a higher frequency of mass movement and debris flow and block the river (Figures 6C, D and 7). This kind of geomorphic processes was also found in the Minjiang and Jinsha Rivers at the margin of the Tibet Plateau (Wang et al., 2007; Chen et al., 2008; Luo et al., 2019; Bao et al., 2020).

The angular boulders at site of ZMD may also indicate earthquakes that shocked and fractured the bedrock at high elevations and triggered a large number of deep-seated bedrock landslides (e.g. Hovius and Stark 2006). Indeed, seven paleo-earthquakes have been identified along the Batang fault (near Yushu) at <22 ka, >14 ka, 14-9.5 ka, 8.0-7.8 ka, >6.7 ka, 4.3-4.0 ka, and <2.7 ka (Huang et al., 2015), which may have produced extreme event deposit (Figure 7). Glacier activities could also have formed glacial dams and block the river in high mountains (e.g. Korup and Tweed, 2007). But it is debated whether there was a large ice sheet during the late Pleistocene in the central and eastern Tibet Plateau, although large numbers of glaciers in high mountains and upstream valleys (such as Queer shan and Bayan Har Shan) have been reported (Kuhle et al., 2004; Stroeven et al., 2009; Shi, 2004). Thus, until now, it is impossible to exclude effects of glacial processes on the extreme events. However, these extreme events could have had high potential contributions to the incision of the more than 1,000 m deep canyon in this area and in other regions, which deserves further study.

6. Conclusion

Sedimentary facies analysis with OSL dating of depositional sequences at seven transects with different relative tectonic activity background along the upper Yangtze River identified terraces of T7-T3 (~19-13 ka), T2 (~9 ka), T1 (~5 ka), respectively. The headwaters of the Yangtze River experienced aggradation from the valley base to up to 62 m apf during the LGM; subsequently, the river transformed to continuous incision with episodic lateral erosion and stability. A set of cut-in-fill terraces has formed as a response to improved climatic conditions with increasing monsoon precipitation and improved vegetation since deglaciation. The relative tectonic activities dominated the distribution pattern and morphologic features of terraces, while the drainage sediment input, directly related to climate change, acted as a primary controlling factor on fluvial processes. In addition, the interbedded debris flows deposits, fluvial deposits and colluvial sediments indicate that climate transformation around 20 ka resulted in alternations of fluvial and slope sediments especially in the gorge area. The latter deposits were episodic and possibly related to earthquakes, climatic transitions, and/or glacial activities. As a result, ephemeral dams could be created with later on occasionally spillovers and outbreaks, and even mega-floods. These geomorphologic processes might lead to extreme fluvial incision and denudation which are characteristic for the geomorphic change and landscape evolution on the Tibet Plateau.

Acknowledgements

Yan Dai, Junfei Ma, Quanxu Hu, Linman Gao, Xun Yang, Bingling Wang, Wanting Xie, and Zhengchen Li are thanked for their help during the fieldwork. This research is supported by the National Natural Science Foundation of China (41971005), Second Tibetan Plateau Scientific Expedition Program (STEP)(2019QZKK0205), and the National Key Research and Development Program (grant number 2016YFA0600500). All of data (including longitudinal profile of the Yangtze River, steepness and precipitation along the Yangtze River, Maximum, minimum and mean

elevation along the upper Yangtze River, De values of each disc for all OSL dating samples in this study and the information of terrace distribution) could be free downloaded from the Zenodo data repository (https://doi.org/10.5281/zenodo.4264700).

References

Allen, P.A. (2008). From landscapes into geological history. *Nature*, *451*, 274-276. https://doi.org/10.1038/nature06586.

Bao, Y.D., Zhai, S.J., Chen, J.P., Xu, P.H., Sun, X.H., Zhan, J.W., Zhang, W. & Zhou, X. (2020). The evolution of the Samaoding paleolandslide river blocking event at the upstream reaches of the Jinsha River, Tibetan Plateau. Geomorphology, 351, 106970. https://doi.org/10.1016/j.geomorph.2019.106970.

Berger, A. & Loutre, M.F. (1991). Insolation values for the climate of the last 10 million years. *Quaternary Science Reviews*, *10*, 297-317. https://doi.org/10.1016/0277-3791(91)90033-Q

Bender, A.M., Amos, C.B., Bierman, P., Rood, D.H., Staisch, L., Kelsey, H., & Sherrod, B. (2016). Differential uplift and incision of the Yakima River terraces, central Washington State. *Journal of Geophysical Research: Solid Earth*, *121*, 365-384. https://doi.org/10.1002/2015JB012303.

Bender, A.M., Lease, R.O., Haeussler, P.J., Rittenour, T., Corbett, L.B., Bierman, P.R., & Caffee, M.W. (2019). Pace and process of active folding and fluvial incision across the Kantishna Hills anticline, central Alaska. *Geophysical Research Letters*, *46*, 3235-3244. https://doi.org/10.1029/2018GL081509.

Bridgland, D.R, Westaway, R. (2008). Preservation patterns of Late Cenozoic fluvial deposits and their implications: results from IGCP 449. *Quaternary International*, *189*, 5-38. https://doi.org/10.1016/j.quaint.2007.08.036.

Busschers, F.S., Kasse, C., Van Balen, R.T., Vandenberghe, J., Cohen, K.M., Weerts, H.J.T., Wallinga, J., Johns, C., Cleveringa, P. & Bunnik, F.P.M. (2007). Late Pleistocene evolution of the Rhine-Meuse system in the Southern North Sea basin: imprints of climate change, sea-level oscillation and glacio-isostacy. *Quaternary Science Reviews*, *26*, 3216-3248. https://doi.org/10.1016/j.quascirev.2007.07.013.

Chahal, P., Kumar, A., Sharma, C.P., Singhal, S., Sundriyal, Y.P. & Srivastava, P. (2019). Late Pleistocene history of aggradation and incision, provenance and channel connectivity of the Zanskar River, NW Himalaya. *Global and Planetary Change*, *178*, 110-128. https://doi.org/10.1016/j.gloplacha.2019.04.015.

Chen, J., Dai, F.C. & Yao, X. (2008). Holocene debris-flow deposits and their implications on the climate in the upper Jinsha River valley, China. *Geomorphology*, *93*, 493-500. https://doi.org/10.1016/j.geomorph.2007.03.011.

Chen, Z.W., Yang, P.X., Li, Z.M. & Li, J.J. (2010). Characteristics of Ms7.1 Yushu earthquake fault and the surface rupture. *Quaternary Sciences, 30*, 628-631. Doi: 10.3969/j.issn.1001-7410.2010.03.24.

Chug, D., Pathak, A., Indu, J., Jain, S. K., Jain, S. K., Dimri, A. P., Niyogi, D., & Ghosh, S. (2020). Observed Evidence for Steep Rise in the Extreme Flow of Western Himalayan Rivers. *Geophysical Research Letters, 46*, e2020GL087815. https://doi.org/10.1029/2020GL087815.

Clark, M.K., Schoenbohm, L.M., Royden, L.H., Whipple, K.X., Burchfiel, B.C., Zhang, X., Tang, W., Wang, E. & Chen, L. (2004) Surface uplift, tectonics, and erosion of eastern Tibet from large-scale drainage patterns. *Tectonics*, *23*, TC1006. https://doi.org/10.1029/2002TC001402.

Clark, M.K., House, M.A., Royden, L.H., Whipple, K. X., Burchfiel, B.C., Zhang, X. & Tang, W. (2005) Late Cenozoic uplift of southeastern Tibet. *Geology*, *33*, p. 525-528. https://doi.org/10.1130/G21265.1.

Clark, M.K., Royden, L.H., Whipple, K.X., Burchfiel, B. C., Zhang, X. & Tang, W. (2006). Use of a regional, relict landscape to measure vertical deformation of the eastern Tibetan Plateau. *Journal of Geophysical Research: Earth Surface, 111*, F03002. https://doi.org/10.1029/2005JF000294.

Cook, K.L., Andermann, C., Gimbert, F., Adhikari, B.R., & Hovius, N. (2018). Glacial lake outburst floods as drivers of fluvial erosion in the Himalaya. *Science, 362*, p. 53-57. doi: 10.1126/science.aat4981.

Chevalier, M., Leloup, P.H., Replumaz, A., Pan, J.W., Metois, M., & Li, H.B. (2017). Temporally constant slip rate along the Ganzi fault, NW Xianshuihe fault system, eastern Tibet. *Geological Society of America Bulletin, 130*, 396-410. https://doi.org/10.1130/B31691.1.

De Paula, B.L.F. & Magalhães Jr, A.P. (2020). Late quaternary landscape evolution in the Atlantic Plateau (Brazilian highlands): Tectonic and climatic implications of fluvial archives. Earth-Science Reviews, 207. https://doi.org/10.1016/ j.earscirev.2020.103228

Duller, G. (2003). Distinguishing quartz and feldspar in single grain luminescence measurements. *Radiation Measurements, 37*, 161–165. https://doi.org/10.1016/S1350-4487(02)00170-1

Duvall, A.R. & Tucker, G.E. (2015). Dynamic ridges and valleys in a strike-slip environment. *Journal of Geophysical Research: Earth Surface, 120*, 2016-2026. https://doi.org/10.1002/2015JF003618

Fan, X.M., Scaringi, G., Korup, O., West, A.J., van Westen, C.J., Tanyas, H., Hovius, N., Hales, T.C., Jibson, R.W., Allstadt, K.E., Zhang, L.M., Evans, S.G., Xu, C., Li, G., Pei, X.J., Xu, Q. & Huang, R.Q. (2019). Earthquake-induced chains of geologic hazards: Patterns, mechanisms, and impacts. *Reviews of Geophysics, 57,* p. 421-503. https://doi. org/10.1029/2018RG000626.

Ferrier, K.L., Huppert, K.L. & Perron, J.T. (2013). Climatic control of bedrock river incision. *Nature, 496*, 206-210. https://xs.scihub.ltd/https://doi.org/10.1038/nature11982.

Fielding, E., Isacks, B., Barazangi, M. & Duncan, C. (1994). How flat is Tibet ?. *Geology, 22(2)*, 163-167. https://doi.org/10.1130/0091-7613(1994)022<0163:HFIT>2.3.CO;2.

Gao, L.M., Wang, X.Y., Yi, S.W., Vandenberghe, J., Gibling, M.R. & Lu, H.Y. (2018). Episodic Sedimentary Evolution of an Alluvial Fan (Huangshui Catchment, NE Tibetan Plateau). Quaternary 1, 16. doi: 10.3390/quat1020016

Guérin, G., Mercier, N. & Adamiec, G. (2011). Dose-rate conversion factors: Update. *Ancient TL, 29*, 5-8.

Han, Z.P., Sinclair, H.D., Li, Y.L., Wang, C.S., Tao, Z., Qian, X.Y., Ning, Z.J., Zhang, J.W., Wen, Y.X., Lin, J., Zhang, B.S., Xu, M., Dai, J.G., Zhou, A., Liang, H.M. & Cao, S. (2019). Internal drainage has sustained low-relief Tibetan landscapes since the early Miocene. *Geophysical Research Letters, 46*, 8741-8752. https://doi.org/10.1029/ 2019GL083019.

Handwerger, A.L., Fielding, E.J., Huang, M.H., Bennett, G.L., Liang, C. & Schulz, W.H. (2019). Widespread initiation, reactivation, and acceleration of landslides in the northern California Coast Ranges due to extreme rainfall. *Journal Geophysical Research: Earth Surface*, *124*, 1782-1797. https://doi.org/10.1029/2019JF005035.

Henck, A.C., Huntington, K.W., Stone, J.O., Montgomery, D.R. & Hallet, B. (2011). Spatial controls on erosion in the Three Rivers Region, southeastern Tibet and southwestern China. *Earth and Planetary Science Letters, 303*, 71-83. https://doi.org/10.1016/j.epsl.2010.12.038.

Hewitt, K., Clague, J.J. & Orwin, J.F. (2008). Legacies of catastrophic rock slope failures in mountain landscapes. *Earth-Science Reviews, 87*, 1-38. https://doi.org/10.1016/j.earscirev.2007.10.002

Heyman, J., Stroeven, A.P., Caffee, M.W., Hättestrand, C., Harbor, J.M., Li, Y.K., Alexanderson, H., Zhou, L.P. & Hubbard, A. (2011). Palaeoglaciology of Bayan Har Shan, NE Tibet Plateau: exposure ages reveal a missing LGM expansion. *Quaternary Science Reviews, 30*, 1988-2001. https://doi.org/10.1016/j.quascirev.2011.05.002

Hovius, N. & Stark, C.P. (2006). Landslide-driven erosion and topographic evolution of active mountain belts. In: Evans SG et al (eds) Landslides from massive rock slope failure. Springer, Berlin, 573–590.

Huang, X.M., Du, Y., He, Z.T., Ma, B.Q & Xie, F.R. (2015). Late Pleistocene–Holocene paleoseismology of the Batang fault (central Tibet plateau, China). *Geomorphology, 239*, 127-141. https://doi.org/10.1016/j.geomorph.2015.03.026.

Johnsen, S.J., Dahl-Jensen, D., Gundestrup, N., Steffensen, J.P., Clausen, H.B., Miller, H., Masson-Delmotte, V., Sveinbjsˇrndottir, A.E. & White, J. (2001). Oxygen isotope and palaeotemperature records from six Greenland ice-core stations: Camp Century, Dye- 3, GRIP, GISP2, Renland and NorthGRIP. *Journal of Quaternary Science, 16*, 299–307. https://doi.org/10.1002/jqs.622.

Kirby, E., Whipple, K.X., Tang, W. & Chen, Z. (2003). Distribution of active rock uplift along the eastern margin of the Tibetan Plateau: Inferences from bedrock channel longitudinal profiles. *Journal of Geophysical Research, 108*, 2217. doi:10.1029/2001JB000861

Kong, P., Na, C.G., Fink, D., Zhao, X.T. & Xiao, W. (2009). Moraine dam related to late Quaternary glaciation in the Yulong Mountains, southwest China, and impacts on the Jinsha River: *Quaternary Science Reviews, 28*, 3224-3235. https://doi.org/10.1016/j.quascirev.2009.08.005

Korup, O. (2006). Rock-slope failure and the river long profile. *Geology, 34*, 45-48. doi: 10.1130/G21959.1.

Korup, O. & Tweed, F. (2007). Ice, moraine, and landslide dams in mountainous terrain. *Quaternary Science Reviews, v. 26*, 3406-3422.

doi:10.1016/j.quascirev.2007.10.012.

Korup, O. & Montgomery, D.R. (2008). Tibetan plateau river incision inhibited by glacial stabilization of the Tsangpo gorge. *Nature, 455,* p. 786-789. https://doi.org/10.1038/nature07322.

Korup, O., Montgomert, D.R. & Hewitt, K. (2010). Glacier and landslide feedbacks to topographic relief in the Himalayan syntaxes. *Proceedings of the National Academy of Sciences of the United States of America*, *107*, 5317-5322. https://doi.org/10.1073/pnas.0907531107

Korup, O., Densmore, A.L. & Schlunegger, F. (2010). The role of landslides in mountain range evolution. *Geomorphology, 120,* 77-90. https://doi.org/10.1016/j.geomorph.2009.09.017.

Kothyari, G.C. & Luirei, K. (2016). Late Quaternary tectonic landforms and fluvial aggradation in the Saryu River valley: Central Kumaun Himalaya. *Geomorphology, 268*, 159-176. https://doi.org/10.1016/j.geomorph.2016.06.010.

Kuhle, M. (2004). The high glacial (last ice age and LGM) ice cover in High and Central Asia. *Indevelopments in Quaternary Sciences, 2*, 175-199. https://doi.org/10.1016/S1571-0866(04)80123-4.

Li, Y.J., Armitage, S.J., Stevens, T. & Meng, X.M. (2018). Alluvial fan aggradation /incision history of the eastern Tibetan plateau margin and implications for debris flow/debris-charged flood hazard. *Geomorphology*, *318*, 203-216. https://doi.org/10.1016/j.geomorph.2018.06.016

Liu, W.M., Lai, Z.P., Hu, K.H., Ge, Y.G., Cui, P., Zhang, X.G. & Liu, F. (2015). Age and extent of a giant glacial-dammed lake at Yarlung Tsangpo gorge in the Tibetan Plateau. *Geomorphology*, *246*, 370-376. http://dx.doi.org/10.1016/j.geomorph.2015.06.034.

Liu, W.M., Hu, K.H., Carling, P.A., Lai, Z.P., Cheng, T. & Xu, Y.L. (2018). The establishment and influence of Baimakou paleo-dam in an upstream reach of the Yangtze River, southeastern margin of the Tibetan Plateau. *Geomorphology*, *321*, 167-173. https://doi.org/10.1016/j.geomorph.2018.08.028.

Liu, W.M., Carling, P.A., Hu, K.H., Wang, H., Zhou, Z., Zhou, L.Q., Liu, D.Z., Lai, Z.P. & Zhang, X.B. (2018). Outburst floods in China: A review. *Earth-Science Reviews, 197,* 102895. https://doi.org/10.1016/j.earscirev.2019.102895

Liu, W., Ju, N.P., Zhang, Z., Chen, Z. & He, S.M. (2020). Simulating the process of the Jinshajiang landslide-caused disaster chain in October 2018. *Bulletin of Engineering Geology and the Environment, 79,* 2189-2199. https://doi.org/10.1007/s10064-019-01717-6

Liu-Zeng, J., Tapponnier, P., Gaudemer, Y. & Ding, L. (2008). Quantifying landscape differences across the Tibetan plateau: Implications for topographic relief evolution. *Journal of Geophysical Research: Earth Surface, 113*, F04018. https://doi.org/10.1029/2007JF000897 F4.

Luo, X.K., Yin, Z.Q. & Yang, L.W. (2019). Preliminary analysis on the development characteristics of river terraces and their relationship with ancient landslides in the reaches of Minjiang River. *Quaternary Sciences, 2*, 391-398. doi: 10.11928/j.issn.1001-7410.2019.02.11

Mejdahl, V. (1979). Thermoluminescence Dating: Beta-dose attenuation in quartz Grains. *Archoeornetry, 21*, 61-79. https://doi.org/10.1111/j.1475-4754.1979.tb00241.x.

Miall, A.D. (1996). The Geology of Fluvial Deposits: sedimentary facies, basin analysis, and petroleum geology. Springer: Berlin-Heidelberg, Germany, ISBN 3-540-59186-9.

Molnar, P., England, P. & Martinod, J. (1993) Mantle dynamics, uplift of the Tibetan Plateau, and the Indian monsoon. *Reviews of Geophysics, 31*, 357-396. https://doi.org/10.1029/93RG02030.

Molnar, P. & Houseman, G.A. (2013). Rayleigh-Taylor instability, lithospheric dynamics, surface topography at convergent mountain belts, and gravity anomalies. *Journal of Geophysical Research: Solid Earth, 118(5),* 2544-2557. https://doi.org/10.1002/jgrb.50203.

Murray, A.S. & Wintle, A.G. (2000). Luminescence dating of quartz using an improved single-aliquot regenerative dose protocol. *Radiation measurements, 32,* 57-73. https://doi.org/10.1016/S1350-4487(99)00253-X.

Murray, A.S. & Wintle, A.G. (2003). The single aliquot regenerative dose protocol: potential for improvements in reliability. *Radiation measurements, 37*, 377-381. https://doi.org/10.1016/S1350-4487(03)00053-2.

Nie, J.S., Ruetenik, G., Gallagher, K., Hoke, G., Garzione, C.N., Wang, W.T., Stockli, D., Hu, X.F., Wang, Z., Wang, Y., Stevens, T., Danišík, M. & Liu, S.P. (2018). Rapid incision of the Mekong River in the middle Miocene linked to monsoonal precipitation. *Nature Geoscience, 11*, 944-948. https://xs.scihub.ltd/https://doi.org/10.1038/s41561-018-0244-z.

Ou, X.J., Lai, Z.P., Zhou, S.Z. & Zeng, L.H. (2014). Timing of glacier fluctuations and trigger mechanisms in eastern qinghai–tibetan plateau during the late quaternary. *Quaternary Research, 81*, 464-475. http://dx.doi.org/10.1016/j.yqres.2013.09.007

Ray, Y. & Srivastava, P. (2010). Widespread aggradation in the mountainous catchment of the Alaknanda-Ganga River System: Timescales and implications to Hinterland-foreland relationships. Quaternary Science Reviews, 29, 2238–2260. https://doi.org/10.1016/j. quascirev.2010.05.023.

Rhoads, B. (2020). River Dynamics: Geomorphology to Support Management. Cambridge. Cambridge University Press. doi:10.1017/9781108164108.

Schuum, S.A. (1993). River Response to baselevel Change: Implications for Sequence Stratigraphy. *The Journal of Geology*, *2*, 279-294. https://doi.org/10.1086/648221.

Sewell, R.J., Parry, S., Millis, S.W., Wang, N., Rieser, U. & DeWitt, R. (2015). Dating of debris flow fan complexes from Lantau Island, Hong Kong, China: The potential relationship between landslide activity and climate change. *Geomorphology*, *248*, 205-227. http://dx.doi.org/10.1016/j.geomorph.2015.07.041.

Sømme, T.O. & Jackson, C.A-L. (2013). Source-to-sink analysis of ancient sedimentary systems using a subsurface case study from the Møre-Trøndel ag area of southern Norway: Part2 – sediment dispersal and forcing mechanisms. *Basin Research*, *25*, 512-531. https://doi.org/10.1111/bre.12014.

Schanz, S.A., Montgomery, D.R., Collins, B.D. & Duvall, A.R. (2018) Multiple paths to straths: A review and reassessment of terrace genesis. *Geomorphology, 312*, 12-23. https://doi.org/10.1016/j.geomorph.2018.03.028.

Shi, Y.F. (2004). The emergence and abandonment of the ice sheet hypothesis over the Qinghal-Xizang Plateau during the ice age. *Quaternary Sciences, 24*, 10-18. doi:10.3321/j.issn:1001-7410.2004.01.002.

Srivastava, P., Tripathi, J.K., Islam, R. & Jaiswal, M.K. (2008). Fashion and phases of latenPleistocene aggradation and incision in the Alaknanda River Valley, western Himalaya, India. *Quaternary Research,. 70*, 68–80. https://doi.org/10.1016/j.yqres.2008.03.009.

Stokes, M., Mather, A.E., Rodes, A., Kearsey, S.H. & Lewin, S. (2018). Anatomy, Age and Origin of an Intramontane Top Basin Surface (Sorbas Basin, Betic Cordillera, SE Spain). *Quaternary 1, 15*. doi: 10.20944/preprints201807.0070.v1.

Stroeven, A.P, Hättestrand, C., Heyman, J., Harbor, J., Li, Y.K., Zhou, L.P., Caffee, M.W., Alexanderson, H., Kleman, J., Ma, H.Z. & Liu, G.N. (2009). Landscape analysis of the Huang He headwaters, NE Tibetan Plateau—Patterns of glacial and fluvial erosion. *Geomorphology, 103*, 212-226. https://doi.org/10.1016/j.geomorph.2008.04.024.

Tao, Y.L., Xiong, J.G., Zhang, H.P., Chang, H. & Li, L.Y. (2020). Climate-driven formation of fluvial terraces across the Tibetan Plateau science 200 kya: A review. *Quaternary Science Reviews, 237*, 106303. https://doi.org/10.1016/j.quascirev.2020.106303.

Thompson, L.O., Yao, T.D., Davis, M.E., Henderson, K.A., Mosley-Thompson, E., Lin, P.N. & Bolzan, J.F. (1997). Tropical climate instability: The last glacial cycle from a Qinghai-Tibetan ice core. *Science*, *276*, 1821-1825. doi: 10.1126/science.276.5320.1821.

Vandenberghe, J., Wang, X.Y. & Lu, H.Y. (2011). Differential impact of small-scaled tectonic movements on fluvial morphology and sedimentology (the Huang Shui catchment, NE Tibet Plateau). *Geomorphology, 134*, 171-185. https://doi.org/10.1016/j.geomorph.2011.06.020.

Vandenberghe, J. (2015). River terraces as a response to climatic forcing: formation processes, sedimentary characteristics and sites for human occupation. *Quaternary International, 370*, 3-11. https://doi.org/10.1016/j.quaint.2014.05.046.

Vandenberghe, J., Kasse, C., Popov, D., Markovic, S.B., Vandenberghe, D., Bohncke, S. & Gabris, G. (2018). Specifying the external impact on fluvial lowland evolution: the last glacial Tisza (Tisa) catchment in Hungary and Serbia. *Quaternary 1, 14*.doi:10.3390/quat1020014.

Wang, L.S., Wang, X.Q., Xu, X.N. & Cui, J. (2007). What happened on the upstream of Minjiang River in Sichuan Province 20000 years ago. *Earth Science Frontiers, 14(4)*,189-196.

Wang, S.F., Fan, C., Wang, G. & Wang, E.C. (2008). Late Cenozoic deformation along the northwestern continuation of the Xianshuihe fault system, Eastern Tibetan Plateau. *Geological Society of America Bulletin, 120*, 312-327. https://doi.org/10.1130/B25833.1.

Wang, X.Y., Lu, H.Y., Vandenberghe, J., Zheng, S.H. & Van Balen, R. (2012). Late Miocene uplift of the NE Tibetan Plateau inferred from basin filling, planation and fluvial terraces in the Huang Shui catchment. *Global and Planetary Change, 88*, 10-19. https://doi.org/10.1016/j.gloplacha.2012.02.009.

Wang, X.Y., Van Balen, R., Yi, S.W., Vandenberghe, J. & Lu, H.Y. (2014). Differential tectonic movements in the confluence area of the Huang Shui and Huang He rivers (Yellow River), NE Tibetan Plateau, as inferred from fluvial terrace positions. *Boreas, 43*, 469-484. https://doi.org/10.1111/bor.12054.

Wang, X.Y., Vandenberghe, J., Yi, S.W., Van Balen, R. & Lu, H.Y. (2015). Climate-dependent fluvial architecture and processes on a suborbital timescale in areas of rapid tectonic uplift: an example from the NE Tibetan Plateau. *Global and Planetary Change, 133*, 318-329. https://doi.org/10.1016/j.gloplacha.2015.09.009.

Wang, X.Y., Vandenberghe, J., Lu, H.Y. & Van Balen, R. (2017). Climatic and tectonic controls on the fluvial morphology of the Northeastern Tibetan Plateau (China). *Journal of Geographical Sciences, 27*, 1325-1340. https://doi.org/10.1007/s11442-017-1438-9.

Wang, Y.Z., Zhang, H.P., Zheng, D.W., Dassow, W.V., Zhang, Z.Q., Yu, J.X. & Pang, J.Z. (2017). How a stationary knickpoint is sustained: New insight into the formation of the deep Yarlung Tsangpo Gorge. *Geomorphology, 285*, 28-43. http://dx.doi.org/10.1016/j.geomorph.2017.02.005.

Wen, X.Z., Xu, X.W., Zheng, R.Z., Xie, Y.Q. & Wan, C. (2003). The average slip rate of Ganzi-Yushu fault and the fragmentation of modern earthquake. *Science China(D), 33*, 199-208. doi: 10.3321/j.issn:1006-9267.2003.z1.022.

Wen, X.Z., Huang, S.M. & Jiang, Z.X. (1985). Neotectonic characteristics and seismic risk assessment of the Ganzi-Yushu fault zone. *Seismology and Geology, 7*, 23-32.

Whipple, K.X., Kirby, E. & Brocklehurst, S.H. (1999). Geomorphic limits to climate-induced increases in topographic relief. *Nature, 401*, 39-43. https://doi.org/10.1038/43375.

Wu, Q.L., Zhao, Z.J., Liu, L., Granger, D.E., Wang, H., Cohen, D.J., Wu, X.H., Ye, M.L., Bar-Yosef, O., Liu, B., Zhang, J., Zhang, P.Z., Yuan, D.Y., Qi, W.Y., Cai, L.H. & Bai, S.B. (2016). Outburst flood at 1920 BCE supports historicity of China's Great Flood and the Xia dynasty. *Science, 353*, 579-582.

doi: 10.1126/science.aaf0842

Wu, Z.H., Zhao, X.T., Fan, T.Y., Ye, P.S., Tong, Y.B., Yang, Z.Y. (2012). Active faults and seismologic characteristics along the Dali-Ruili railway in western Yunnan Province. *Geological Bulletin of China, 31*, 191-217.

Yang, R., Willett, S.D. & Goren, L. (2015). In situ low-relief landscape formation as a result of river network disruption. *Nature, 520*, 526-529. https://doi.org/10.1038/nature14354.

Yu, Y., Wang, X.Y., Li, Y.Q., Dai, Y. & Lu, H.Y. (2018). The evolution of drainage pattern and its relation to tectonic movement in the upstream Yangtze catchment. *Acta Geographica Sinica, 73*, 1338-1352. http://www.geog.com.cn/CN/10.11821/dlxb201807012.

Zhang, G.H., Shan, X.J., Delouis, B., Qu, C.Y., Balestra, J., Li, Z.H., Liu, Y.H. & Zhang, G.F. (2013). Rupture history of the 2010 Ms 7.1 Yushu earthquake by joint inversion of teleseismic data and InSAR measurements. *Tectonophysics*, *584*, 129-137. doi:10.1016/j.tecto.2012.03.024.

Zhang, H.P., Oskin, M.E., Liu-Zeng, J., Zhang, P.Z., Reiners, P.W. & Xiao, P. (2016). Pulsed exhumation of interior eastern Tibet: Implications for relief generation mechanisms and the origin of high-elevation planation surfaces. *Earth and Planetary Science Letters*, *449*, 176-185. https://doi.org/10.1016/j.epsl.2016.05.048.

Zhang, J.Y., Liu-Zeng, J., Scherler, D., Yin, A., Wang, W., Tang, M.Y. & Li, Z.F. (2018). Spatiotemporal variation of late Quaternary river incision rates in southeast Tibet, constrained by dating fluvial terraces. *Lithosphere*, *10*, 662–676. https://doi.org/10.1130/L686.1.

Zhao, Y., Tzedakis, P.C., Li, Q., Qin, F., Cui, Q.Y., Liang,C., Birks, H.B., Liu, Y.L., Zhang, Z.Y., Ge, J.Y., Zhao, H., Felde, V.A., Deng, C.L., Cia, M.T., Li, H., Ren, W.H., Wei, H.C., Yang, H.F., Zhang, J.W., Yu, Z.C. & Guo, Z.T. (2020). Evolution of vegetation and climate variability on the Tibet Plateau over the past 1.74 million years. *Science Advances, 6(19)*, essay6193. doi: 10.1126/sciadv.aay6193.

Zhou, R.J., Ma, S.H. & Cai, C.S. (1996). Late Quaternary active features of the Ganzi–Yushu fault zone. Earthquake Research in China, 12, 250–260.

Zhou, R.J., Wen, X.Z., Cai, C.X. & Ma, S.H. (1997). Recent earthquakes and assessment of seismic tendency on the Ganzi-Yushu fault zone. *Seismology and Geology*, *19*, 115-124.

Zhou, R.J., Li, Y., Liang, M.J., Xu, X.W., He, Y.L., Wang, S.Y., Ma, C. & Liu, Y.F. (2014). Determination of mean recurrence interval of large earthquakes on the Garzê-Yushu Fault (Dengke Segment) on the eastern margin of the Qinghai-Tibetan Plateau. *Quaternary International, 30*, 1-9. http://dx.doi.org/10.1016/j.quaint.2013.11.010.